THESIS FOR THE DEGREE OF LICENTIATE OF ENGINEERING

Microstructure of Carbon Fibres for Multifunctional Composites: 3D Distribution and Configuration of Atoms

MARCUS JOHANSEN

Department of Industrial and Materials Science
CHALMERS UNIVERSITY OF TECHNOLOGY
Gothenburg, Sweden 2021

Microstructure of Carbon Fibres for Multifunctional Composites:
3D Distribution and Configuration of Atoms
MARCUS JOHANSEN

Department of Industrial and Materials Science
Chalmers University of Technology
SE-412 69 Gothenburg
Sweden
Telephone: +46 (0)31-772 1000

Printed by Chalmers Reproservice
Gothenburg, Sweden 2021

Microstructure of Carbon Fibres for Multifunctional Composites:
3D Distribution and Configuration of Atoms
MARCUS JOHANSEN
Department of Industrial and Materials Science
Chalmers University of Technology

Abstract

Lightweight energy storage is a must for increased driving range of electric vehicles. “Mass-less” energy storage can be achieved by directly storing energy in structural components. In such multifunctional devices called structural composite batteries, carbon fibres carry mechanical load and simultaneously act as negative battery electrode by hosting lithium ions in its microstructure. Little is known of how the microstructure of carbon fibres is optimised for multifunctionality, and deeper understanding of the configuration and the distribution of atoms in carbon fibres is needed.

Here synchrotron hard X-ray photoelectron spectroscopy and atom probe tomography are used to reveal the chemical states and three-dimensional distribution of atoms in commercial carbon fibres. This thesis presents the first ever guide for how to perform atom probe tomography on carbon fibres, and the first ever three-dimensional atomic reconstruction of a carbon fibre.

The results show that the chemical states and distribution of nitrogen heteroatoms in carbon fibres affect the electrochemical performance of the fibres. Carbon fibres performed electrochemically better with higher amount of nitrogen with pyridinic and pyrrolic configurations. Additionally, the nitrogen concentration varies throughout the carbon fibre, which may suggest that the electrochemical properties also vary throughout the carbon fibre. The knowledge provided by this thesis can lead to future carbon fibre designs with enhanced electrochemical performance for multifunctional applications.

Keywords: carbon fibres, multifunctional composites, energy storage, microstructure, heteroatoms, synchrotron hard X-ray photoelectron spectroscopy, atom probe tomography

Preface

The work in this thesis was carried out from June 2019 to June 2021 at the Division of Materials and Manufacturing, Department of Industrial and Materials Science, Chalmers University of Technology. The research was financially supported by Energimyndigheten under project number 46598-1.

Acknowledgements

I would like to wholeheartedly express my gratitude to my supervisor, Associate Professor Fang Liu, for her inexhaustible support and guidance through my stumbling first years in the world of research. These two years have been so joyful, rewarding, and inspiring thanks to her efforts to enrich every step in my journey. She has spent countless hours teaching me how to prepare specimens and conduct experiments; she has helped me innumerable times to make sense of confusing results; and she has read and commented kilometres of my draft texts. PhD studies are at times challenging, but with Fang's support, these times have never been difficult. Thank you, Fang, you are a fantastic supervisor!

I'm also grateful for my co-supervisor, Professor Leif Asp, who many years ago sparked my interest in carbon fibre composites and continuously is a source of inspiration for how to enthusiastically conduct research. He has provided and entrusted me so many opportunities to broaden my knowledge of carbon fibre composites and structural battery composites.

Moreover, I want to thank the rest of the multifunctional composites team at Chalmers and KTH. Multifunctional materials require a multi-competent team. Thank you for sharing your expertise and knowledge. Special thanks to Professor Mats Johansson and Professor Stephan Volkher Roth for their help in organising beam time at PETRA III.

I also want to say thank you to all friends and colleagues at the Department of Industrial and Material Science. Special thanks go to Dr. Erik Tam for his support regarding photoelectron spectroscopy.

Finally, I want to thank my girlfriend Sofie and my family and friends for always cheering me on and at least seeming interested in my work. Thank you for all your tricky questions that strain my knowledge and ability to pedagogically explain. You ground me in the world outside of work. I want you to know how much I appreciate your endless love!

Thesis

This thesis consists of a summary of the research performed and the following appended papers:

Paper I Marcus Johansen, Fang Liu "Best practices for analysis of carbon fibres by atom probe tomography" *Submitted*

Paper II Marcus Johansen, Christoph Schlueter, Pui Lam Tam, Leif E. Asp, Fang Liu "Mapping nitrogen heteroatoms in carbon fibres using atom probe tomography and photoelectron spectroscopy" *Carbon* (2021)

Contribution to the appended papers:

Paper I: Fang Liu suggested the approach. Marcus Johansen executed the majority of the experimental work and analysis of the results. Marcus Johansen and Fang Liu wrote the paper.

Paper II: Fang Liu suggested the approach. Marcus Johansen executed the majority of the atom probe tomography experiment and analysis. Pui Lam Tam executed the X-ray photoelectron spectroscopy experiments, Christoph Schlueter executed the hard X-ray photoelectron spectroscopy experiments, and Marcus Johansen analysed the results. Marcus Johansen and Fang Liu wrote the paper. Leif Asp, Pui Lam Tam, and Christoph Schlueter proof-read the paper and contributed with suggestions and comments.

Contents

List of Abbreviations

APT	atom probe tomography
EELS	electron energy loss spectroscopy
EV	electric vehicle
FIB	focused ion beam
FWHM	full width at half maximum
HAXPES	synchrotron hard X-ray photoelectron spectroscopy
HM	high modulus
ICEV	internal combustion engine vehicle
ID	information depth
IM	intermediate modulus
IMFP	inelastic mean free path
PAN	polyacrylonitrile
SEM	scanning electron microscopy
TEM	transmission electron microscopy
ToF	time of flight
XPS	X-ray photoelectron spectroscopy

1 Introduction

This chapter introduces the thesis by first motivating the aim of deeper fundamental knowledge on the microstructure of carbon fibres. Then the steps to reach that aim are characterised as research objectives and connected to the appended research papers. Finally, the scope for the research is formulated.

1.1 Motivation

Through technological development we humans gradually seize more and more power to transform our environment and improve our living conditions. Many times, the transformation is irreversible, leaving the world for ever altered. We are a part of the natural world, and thus any alteration to it has consequences for our ability to meet our needs today as well as over decades, centuries, and millenniums from now. If we are to thrive in the future, the world and its resources must be sustained.

Energy is an essential resource for human needs, and consumption of finite energy resources like fossil fuel compromises the ability of people now and in the future to meet their needs by depleting natural resources and polluting the environment. Renewable energy resources, on the other hand, can be used today without leaving less for tomorrow. However, renewable energy only has value if we can make use of it in our development activities.

Transport is a cornerstone of society. It is also one of the largest sectors when it comes to energy demand and CO_2 emissions, thus the choice of energy in the transport sector is extremely impactful on sustainability. The electric vehicle (EV) have been proclaimed the successor to the internal combustion engine vehicle (ICEV) to shift the choice away from fossil fuels and towards renewable energy. Still, there are several obstacles for the EV to overcome before dethroning the ICEV. Perhaps the greatest drawback of current EVs, compared to ICEVs, is the inferior driving range, which is limited by energy storing capacity of the EV.

The energy storage system of an EV is typically lithium-ion batteries. The capacity can of course be improved by upsizing the battery pack, but this will not necessarily increase the range of the EV as a bigger battery weighs more,

and greater vehicle mass increases energy consumption. Instead, focus can be laid on making the vehicle lighter by introducing lighter materials like carbon fibre composites in the structural frame, thus reducing energy consumption and improving the vehicle's range. But this is not enough since it does not change the fact that one of the heaviest (i.e. most energy consuming) subsystems in the EV still is the battery pack. For example, ~25% of the weight of a Tesla model S, and ~20% of the weight of a BMW i3 comes from the battery [1], [2]. Lightweight energy storage is thus a must to keep pace with the absolute necessity for electrification in the transport industries [3], [4].

How can the weight of the energy storage system of the EV be reduced? The most obvious way is to increase the specific energy of the battery cell with technologies like lithium-sulphur batteries. Another, less apparent, way is to integrate the energy-storing function of the battery system into the structural system, forming a multifunctional device such as the structural battery composite [5], [6]. In other words, the roof of a car or the wing of an aircraft can store energy, creating a so-called "mass-less energy storage". The mass of the single multifunctional system ($m_{structural\ battery}$) can be lower than the cumulative mass of the multiple monofunctional systems ($m_{structure} + m_{battery}$).

The structural battery composite merges the functions and constituents of the carbon fibre composite and the lithium-ion battery (Figure 1.1), two fields that are further explored in the coming chapter. The contact point between these fields, and the interface on which the concept of the structural battery composite hinges, is the use of carbon material. In the commercial lithium-ion battery, the most common negative electrode material is graphite, whereas the reinforcement material in high-performance lightweight composites is carbon fibre. In the structural battery composite, carbon fibres act simultaneously as reinforcement and negative electrode. This introduces demands on the carbon fibre to perform not only its traditional role of carrying mechanical load, but also the role of storing electrochemical energy by hosting lithium ions in its microstructure.

The microstructure of the carbon fibre governs both the mechanical and electrochemical properties. Hence, in order to improve the structural battery composite technique, knowledge of the structure-property relationship is a necessity. There have been many studies on this topic [7]–[16], but there is still fundamental knowledge missing regarding the configuration and the

distribution of the atoms that make up the carbon fibre. This knowledge is crucial to truly understand and control the multifunctionality of the carbon fibre. To reveal information about configuration and distribution of atoms, cutting-edge techniques are required. Thus, this thesis explores the carbon fibre by synchrotron hard X-ray photoelectron spectroscopy (HAXPES) and atom probe tomography (APT).

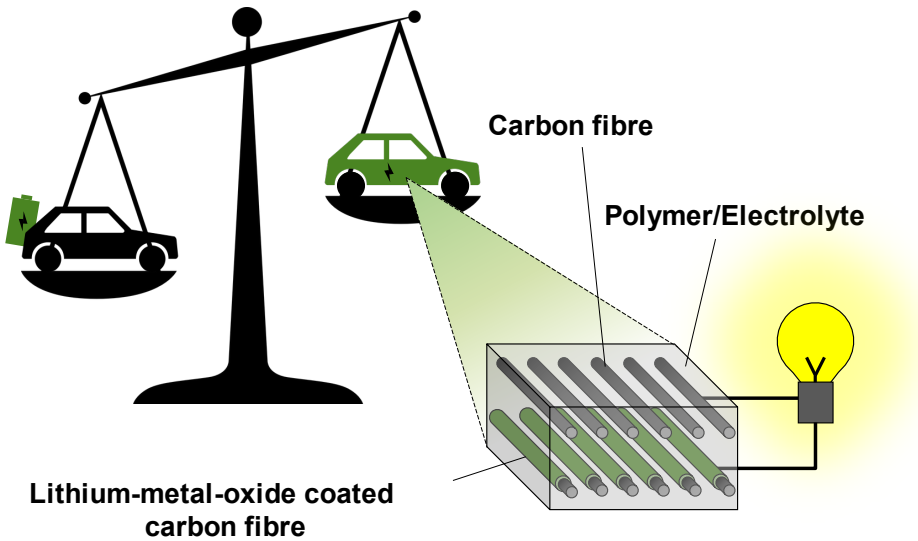

Figure 1.1: Conceptual schematic of a structural battery composite.

1.2 Aim and objectives

The aim of this research is to provide a fundamental understanding of the structure of carbon fibres, and to elucidate the relation between structure and electrochemical properties of carbon fibres. To achieve this aim, the research can be broken down into the following concrete objectives:

- Develop the methodology of performing APT on carbon fibres and interpret the obtained results. This methodology is described in **Paper I**.
- Determine the three-dimensional distribution of individual atoms in carbon fibres using APT. This is presented in **Paper II**.
- Determine the chemical configuration of atoms in carbon fibres by synchrotron HAXPES. This is presented in **Paper II**.
- Correlate the distribution and chemical configuration of atoms in carbon fibres to electrochemical properties. This is presented in **Paper II**.

1.3 Scope

Even though carbon fibres are produced from several different precursor materials, this thesis is only concerned with polyacrylonitrile (PAN) based carbon fibres. The reason behind this delimitation is that the majority of carbon fibres are PAN based and previous research related to structural battery composites has identified PAN based carbon fibres as the most suitable for multifunctional applications. The author has not manufactured the carbon fibres investigated but analysed commercial ones. Furthermore, the author has not performed any mechanical or electrochemical characterisation, but instead relied on recent research for data on electrochemical performance and data sheets from the manufacturer for physical properties of the investigated carbon fibres.

2 Background

This chapter discusses the widely different fields of carbon fibre composites and lithium-ion batteries, and how they are merged in the field of structural battery composites. The link between the fields is the carbon fibre, which is also presented in this chapter regarding its manufacturing, microstructure, and properties.

2.1 Carbon fibre composites

A composite material consists of two or more distinct materials with significantly different properties, that are combined to form a single material entity with better performance than the individual constituents. For structural applications, one or more discontinuous phases are embedded in a continuous phase, where the discontinuous phase, the reinforcement, has better mechanical properties than the continuous phase, the matrix [17]. The matrix fixates the reinforcement in favourable arrangements to transfer external load to the reinforcement and shield the reinforcement from hazardous environments.

The reinforcement can be of the fibrous type, and as the properties of a fibre composite are better in the direction of the fibre, the orientation of the fibres is crucial for the behaviour of the composite. Fibre composites often consist of layers stacked to form a laminate, where the fibres in each layer have the same orientation, but, depending on what behaviour is sought, the layers can be stacked with different orientation relative to each other (Figure 2.1). Fibre composites are thus typically anisotropic.

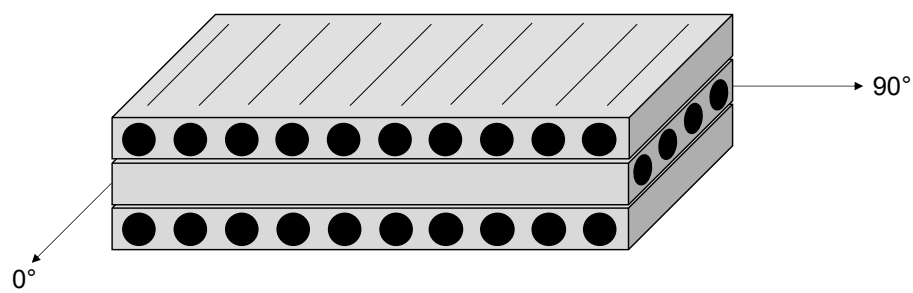

Figure 2.1: Fibre composite laminate with upper and lower layers in the 0° direction, and the middle layer in the 90° direction.

The material of the fibre and the matrix can vary widely, but in lightweight applications the fibre material usually is carbon, glass, or aramid, and the matrix material is thermosetting or thermoplastic polymer. Carbon fibre reinforced polymer composites have excellent modulus-to-density ratio (specific modulus) and strength-to-density ratio (specific strength) of around 55 MNm/kg and 240 kNm/kg compared to aluminium 2024-T4 of around 27 MNm/kg and 150 kNm/kg [17]. This makes carbon fibre composites suitable for lightweight aerospace, automotive, naval, storage tank, and wind turbine applications, but also for sporting goods like sports cars, fishing rods, tennis rackets, and golf clubs.

From the perspective of multifunctionality, the carbon fibre composite provides not only a lightweight solution, but also the opportunity for several functions to be spread over the different constituents. Thus, the multi-phase system of the carbon fibre composites is suitable for structural batteries, as the similarities with the lithium-ion battery, covered in next section, facilitates compatibility.

2.2 Lithium-ion batteries

Lithium (Li) is the third element in the periodic system. As the second element of Group 1, it is small, light, and reactive. These properties position Li as an attractive element for use in high-energy density electrochemical cells. The small radius (0.76 Å) allows Li-ions to easily insert into electrode materials, the low density (0.54 kg/dm^3) contributes to high energy per weight unit, and the low electric potential (–3.04 V vs. H_2/H^+) enables high cell voltage.

A Li-ion battery is a type of secondary battery, i.e. rechargeable battery, with high volumetric and gravimetric energy density, that make them suitable for powering weight and volume sensitive electric devices ranging from mobile phones to vehicles. The Li-ion battery converts chemical energy into electrical energy, or vice versa, through reversible oxidation-reduction reactions. Typically, the cell potential range is 2.5-4.5 V [18]. In a Li-ion battery setup (Figure 2.2), the positive electrode is typically a lithium-containing transition metal (manganese, iron, cobalt, or nickel) oxide, and the negative electrode is often carbon-based material (soft carbons, hard carbons, or graphite) [18]. The electrodes are connected by an external electrical circuit and placed on either side of an electron-insulating separator in an ion-conducting electrolyte. During charging the input energy through the external circuit forces Li-ions to be transported from the positive electrode through the separator and inserted into the carbonaceous microstructure of the negative electrode via the electrolyte.

During discharging the Li-ions return spontaneously from the negative electrode to the positive electrode and energy is released.

The negative electrode must have a material structure able to host and release Li-ions. Graphite, which is the most common material for negative electrodes, has a crystal structure of hexagonally arranged carbon (C) atoms in graphene layers bound by weak van der Waals forces. The graphene layers are stacked in an ABA order (Figure 2.3a). Li can be inserted in the interstitial space between the graphene layers to a maximum of one Li-ion per C hexagon, and thus form LiC_6 with a theoretical capacity of 372 mAh/g. The insertion changes the stacking order of the graphene layers to AAA (Figure 2.3b). A disordered stacking of graphene layers, turbostratic structure (Figure 2.3c), can drastically inhibit Li-ion insertion and reduce the capacity [18]. On the opposite end of the scale to graphite lays the disordered hard carbon, which consists of nonparallel graphene layers that do not form stacks. The random inclination of the graphene layers allows Li-ions to bond in porosities and on either side of the layer (Figure 2.3d), and form Li_2C_6 with the theoretical maximum capacity of 740 mAh/g [19]. However, the porosities can trap lithium and lead to irreversible capacity losses.

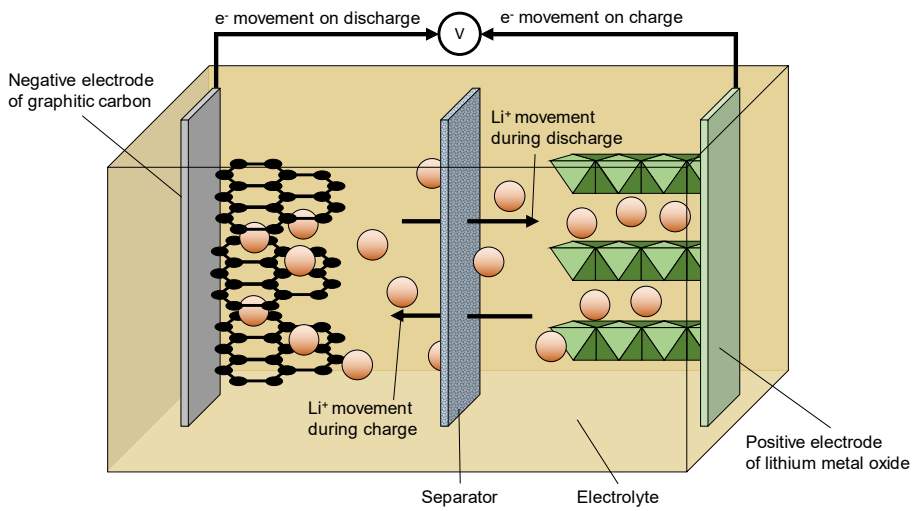

Figure 2.2: Schematic of a lithium-ion battery.

To boost the electrochemical capacity, carbon materials can be doped with heteroatoms like nitrogen (N) [20]. Both N-doped graphene and N-doped mesocarbon microbeads have showed enhanced reversible capacity compared to their pristine counterparts [21], [22]. When N is doped into the carbon network, it can configure in various chemical states (Figure 2.4) that affect the electrochemical properties differently. Graphitic-N is a configuration that substitutes a carbon atom for a nitrogen atom that form bonds with three neighbouring carbon atoms in the graphene layer. Since the N atom has one more electron than the C atom, an extra electron is introduced in the graphene layer leading to a n-type doping and increased electronic conductivity [23]. This can be utilised for faster charging and discharging. However, the n-type doping can be cancelled out by p-type doping from other N configurations of pyridinic-N and pyrrolic-N [24]. Pyridinic-N bonds with two carbon atoms in a six-membered ring, and the pyrrolic-N also bonds with two carbon atoms, but in a five-membered ring. By not bonding to three carbon atoms, pyridinic-N and pyrrolic-N create vacancies and edges in the graphene plane. The defects act as active sites for Li adsorption, and thus increase the capacity of the carbon material [25]–[28].

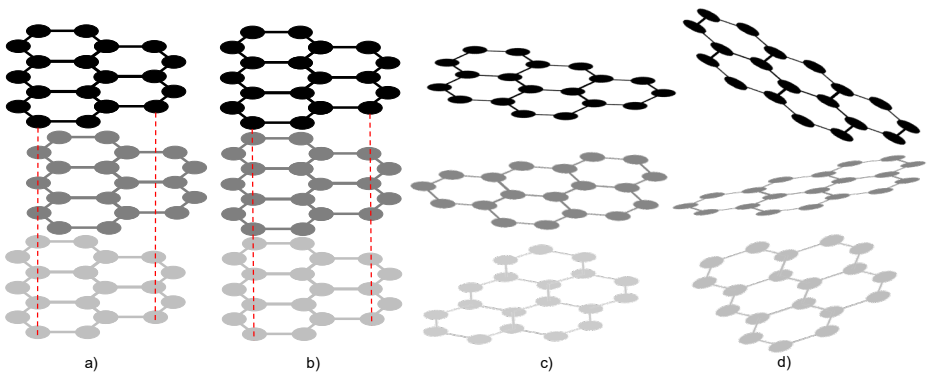

Figure 2.3: a) Graphitic carbon with ABA stacking, b) graphitic carbon with AAA stacking after Li insertion, c) turbostratic carbon, and d) disordered hard carbon.

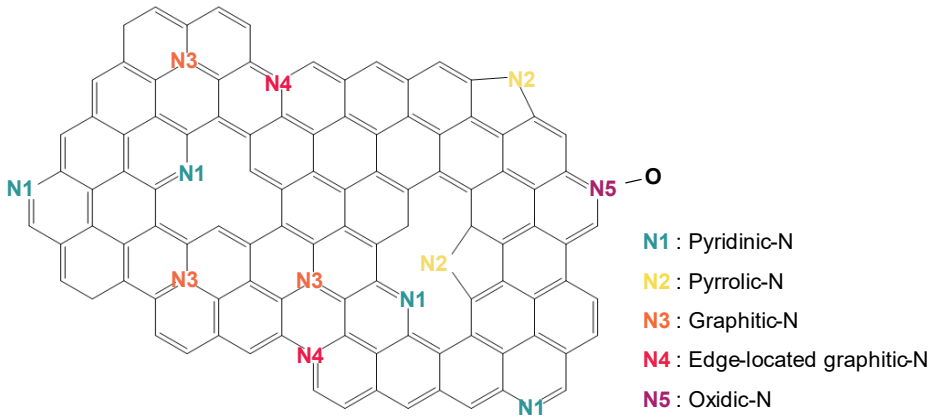

Figure 2.4: Configurations of N heteroatoms in carbon materials. Adapted from Ref. [29]. CC BY 4.0.

2.3 Structural battery composites

The history of the structural battery composite starts in 2007 [5] when researchers at US Army Research Laboratory tried to build a laminated structural battery composite using carbon fibres as negative electrode, a metal mesh as positive electrode, and a glass fibre weave as separator [30]. Even though the mechanical performance was encouraging, the electrochemical performance was low due to insufficient electrical insulation. In 2009, Liu *et al.* attempted to make a structural battery composite with short fibres and a gel electrolyte, which resulted in good electrochemical performance, but poor mechanical performance [31]. In the following years, significant strides were made towards making a truly multifunctional structural battery composite with high mechanical and electrochemical performance [5]. In 2021, Asp *et al.* presented a structural battery composite with up until then unprecedented multifunctional performance of energy density at 24 Wh/kg, elastic modulus of 25 GPa, and tensile strength beyond 300 MPa [32].

The structural battery composite can be made in different architectures. The one presented by Asp *et al.* is a laminated architecture, where a thin unidirectional carbon fibre tow and an aluminium foil coated with lithium-iron-phosphate ($LiFePO_4$) are separated by a thin glass fibre fabric and held by a structural battery electrolyte. The carbon fibres act as reinforcement, negative electrode, and current collector. The lithium source is the positive electrode ($LiFePO_4$) and the glass fibre fabric is the separator. The structural battery electrolyte is a

sponge-like system of a porous solid polymer (for mechanical load transfer) filled with a liquid electrolyte (for ion conduction). Further development of the laminated battery architecture involves replacing the lithium-metal-oxide coated aluminium foil with cathode powder coated carbon fibres (Figure 2.5a). This will allow for increased mechanical performance, weight reduction, and even improved electrochemical stability [33]. Another architecture conceived is the 3D battery architecture (Figure 2.5b). Here each fibre is coated with a structural electrolyte, and positive electrode particles are dispersed in the composite matrix, thus making each coated fibre an individual battery cell.

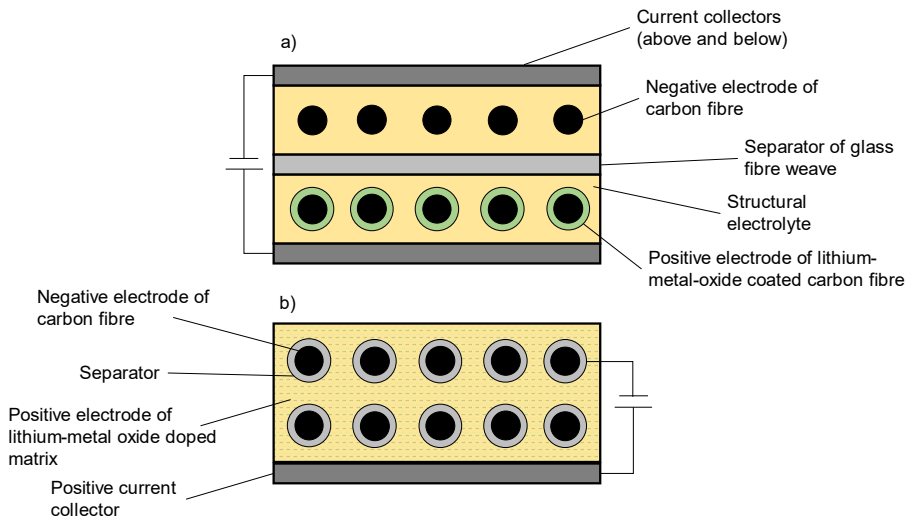

Figure 2.5: Schematic representation of a structural battery composite with a) laminated architecture and b) 3D architecture.

2.4 Carbon Fibres

Carbon fibres are used as reinforcement in lightweight composite materials in a wide spectrum of applications: aircrafts, road vehicles, seafaring vessels, sporting goods, storage tanks, and wind turbines. The global carbon fibre demand is projected to reach 117 kilo tonnes by 2022 [34] on a market comprised of eight companies where some of the largest are Toray, Teijin, and Mitsubishi. Manufacturing of carbon fibres is a complex and fine-tuned process, and thus surrounded by much secrecy that limits public knowledge regarding the relationship between process and properties of the carbon fibres [35].

The typical carbon fibre consists of at least 92 wt% C [36], the rest being N and oxygen (O). The diameter is generally ~5-7 µm. In recent years, the ability of the carbon fibre to store electrochemical energy as battery electrode, and

simultaneously carry mechanical load, has intensified the research on carbon fibres [5]. Traditionally carbon fibres are exclusively used as structural reinforcement due to their excellent specific strength and stiffness. Further recognised properties are excellent creep resistance, high thermal and chemical stability, and good thermal and electrical conductivity [35]. The properties of a carbon fibre are governed by the microstructure, which in turn is governed by the manufacturing.

2.4.1 Manufacturing of carbon fibres

To understand the carbon fibre, it is suitable to start with the precursor material, which ideally is easy to convert to carbon fibre, has a high carbon yield and allows for cost-effective processing. Examples of precursors are rayon, polyacrylonitrile (PAN), pitch, and lignin. Rayon was initially used to make carbon fibres but was soon surpassed by alternatives like PAN and pitch due to their lower production cost [37]. Pitch allows for manufacture of ultra-high modulus fibres, that are relatively brittle, whereas PAN-based carbon fibres can reach a better balance between stiffness and strength. Today the majority of carbon fibres are PAN-based [38], but since the production is expensive and relies on finite resources, attempts are made to make carbon fibres out of the plant-based polymer of lignin. However, PAN-based carbon fibres have proved to be the most suitable type for structural battery composites [39], and therefore this thesis focuses solely on PAN-based carbon fibres.

Acrylonitrile, with chemical formula of CH_2CHCN, is converted into carbon fibres through multiple steps: polymerisation, spinning of fibres, thermal stabilisation, carbonisation, and graphitisation. During polymerisation, monomeric units of acrylonitrile are linked together into PAN chains. To improve processability, 2-15% of comonomer are added. When the precursor material is spun into fibres, the PAN chains are aligned in the fibre direction and stretched [35], [37], [38], [40], [41]. The chain length and alignment influence the final properties of the carbon fibre. At this stage the carbon content in the precursor fibre is 50-60% and the diameter ~15 μm [35], [40].

Fusing the chains into stiff and strong graphene layers requires high temperature treatment, but the PAN chains are thermally instable and therefore need to be stabilised through oxidation at temperatures between 200 and 300°C. The fibre passes through an oxidising atmosphere in an oven with zones of increasing temperature. The oxidation cyclises the chains into thermally stable heteroaromatic ladder structures [37], [38] (Figure 2.6a). After the oxidation,

the fibre consists of 62–70 wt% C, 20–24 wt% N, 5–10 wt% O, and 2–4 wt% hydrogen (H), and the fibre density has increased [38].

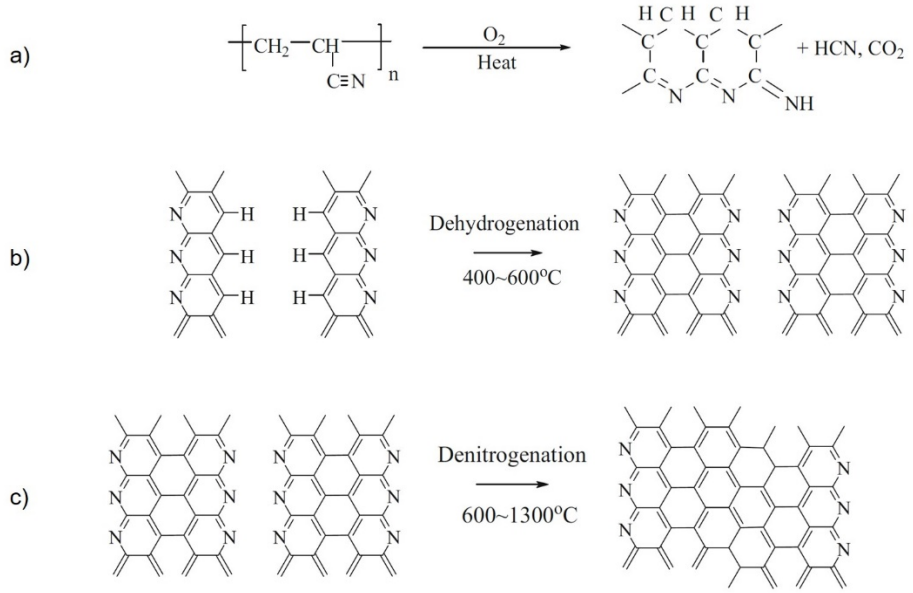

Figure 2.6: Schematic representation of a) cyclisation of PAN via oxidation into heteroatomic ladder structures, that are then b) cross-linked via dehydrogenation into ribbon structures, and finally c) fused via denitrogenation into graphene-like sheets. Adapted from Ref. [35] with permission from Springer Nature.

The stabilised precursor fibre can now withstand high temperatures, and is converted into a carbon fibre through carbonisation and graphitisation: thermal pyrolysis in steps up to around 1600°C and 3000°C. Inert atmosphere must be used to avoid oxidation, and the media for carbonisation is often nitrogen gas (N_2). During carbonisation, much of the non-carbon atoms are expelled in the form of HCN, H_2O, O_2, H_2, CO, NH_3, and CH_4, and the fibre diameter shrinks to ~5-7 μm [35], [41]. Initially, during the first heating zone at 400-600°C, dehydrogenation and elimination of hydroxyl groups lead to cross-linking of the ladder structures into wider ribbon structures bound by nitrogen (Figure 2.6b). In the second heating zone at 600-1600°C, denitrogenation cross-links the ribbon structures into graphene-like sheet structures (Figure 2.6c) in small crystallites. Even though much of the non-carbon atoms are expelled, some still remain: N and O. Depending on the requisite properties of the carbon fibre, carbonisation may be the final heat treatment. Otherwise, graphitisation can be conducted, where the final heat treatment temperature for graphitisation is up to about 3000°C. However, at such elevated temperatures, nitrogen gas cannot be

used as atmosphere, as it will react with the carbon fibre. Instead argon can be used. During graphitisation even more non-carbons are expelled, the crystallites grow, and the alignment of the crystallites is increased [37].

The final step of manufacturing is surface treatment to improve the bond between fibre and polymer matrix. The fibres are coated with a thin polymer layer, sizing, that is supposed to protect the fibre from surface damage, ease handling, and increase the compatibility with the matrix.

2.4.2 Microstructure

The microstructure of carbon fibres is heterogenous, containing crystalline and amorphous domains with ubiquitous nano-pores. In the crystallites, the graphene layers formed during carbonisation are stacked in a turbostratic structure. The basal planes of hexagonal networks are more or less aligned with the axial direction of the fibre and exhibit in-plane long range order, whereas the stacking sequence, unlike the ABA order in a graphitic structure, is disordered [35], [37]. The graphene layers consist of sp^2-hybridised carbon atoms with one of nature's strongest bonds at ~5.9 eV [42], while the binding between the layers is the relatively weak bond of van der Waals forces [37]. In the crystallites, the structure and the bond strength are thus anisotropic.

Many analysis techniques have been deployed to investigate the microstructure of carbon fibres. Among them are techniques like X-ray diffraction [7], [11], [13], [15], [16], [43], Raman spectroscopy [15], [44], and transmission electron microscopy (TEM) [7]–[9], [14], [16], [44]–[46]. These techniques are typically used to characterise the crystallites and amorphous domains in carbon fibres and relate them to mechanical properties. The size of the crystallites is described by the longitudinal length L_a and the thickness of the graphene stack L_c. The interlayer distance in the crystallites, d_{002}, is a measure of the degree of graphitisation. A decreasing value approaching the interlayer distance of pure graphite of 3.35 Å indicates a higher degree of graphitisation. Additional important parameters are the orientation of the crystallites relative the fibre axis and crystallinity. Higher final heat treatment gives larger, more aligned, and more graphitised crystallites [37].

Techniques instead used to determine the composition and distribution of atoms in carbon fibres are for instance X-ray photoelectron spectroscopy (XPS) [37], [47] and electron energy loss spectroscopy (EELS) [45], [46]. The major elements detected are C, O, and N. XPS was mostly used to investigate the

lateral surface and adhesion properties of carbon fibres to increase compatibility with matrix materials in composites [37]. Angle resolved XPS was also used to examine the atomic composition across the cross-section of carbon fibres [47]. Regular XPS can distinguish chemical states of atoms, but at low amounts of an element, such as the relatively low levels of N in carbon fibres, the sensitivity and resolution are insufficient to allow clear chemical state analysis. High in-plane spatial resolution on carbon fibres has been achieved with EELS [45], [46]. However, EELS does not give information on spatial distribution in three dimensions, instead it compresses the information in the thickness direction, and gives information in two dimensions. To reveal three-dimensional atomic distribution and the chemical state of all elements in carbon fibres, the work behind this thesis has included atom probe tomography and synchrotron hard X-ray photoelectron spectroscopy (detailed in Chapter 3).

2.4.3 Properties

The crystallite size and orientation influence the mechanical properties of a carbon fibre. Larger crystallites and greater alignment with the fibre axis yield higher axial tensile modulus [43]. However, due to the anisotropic microstructure of carbon fibres, the transverse modulus can be approximately 10-30 times lower than the axial modulus [48]. Even though graphene is the strongest material ever discovered, the tensile strength of a carbon fibre is many times lower since the strength is compromised by flaws in the microstructure. As larger crystallites have higher risk of inducing critical flaws, carbon fibres with smaller crystallites usually have higher tensile strength [41], [43].

Carbon fibres can be divided, based on their tensile modulus, into at least two types: intermediate modulus (IM) fibres with modulus <300 GPa and high modulus (HM) fibres with a modulus >300 GPa. The final heat treatment of IM fibres is carbonisation up to 1600°C, and thus the IM fibres have relatively small crystallites and high tensile strength (strength-to-modulus ratio greater than 1%). The final heat treatment of HM fibres is graphitisation up to 3000°C, which makes the HM fibres grow bigger crystallites, but the tensile strength is reduced (strength-to-modulus ratio smaller than 1%) [35], [44].

Thermal and electrical conductivity are also affected by the orientation and size of crystallites. HM fibres, with their large and aligned crystallites, have higher thermal conductivity and electrical conductivity than IM fibres [49]. The anisotropic microstructure of carbon fibres allows for very high thermal conductivity in the plane, but poor interplanar conductivity [50], [51].

Carbon fibres can host lithium ions in its microstructure, and thus act as battery electrode [5]. The theoretical maximum capacity of graphite (the most common negative electrode material) is 372 mAh/g, where lithium ions are intercalated between the graphene layers. One might expect that the more crystalline HM fibres with crystallites with higher degree of graphitisation have higher capacity than IM fibres, but the opposite is true. IM fibres have electrochemical capacity up to around 360 mAh/g, compared to the capacity of the HM fibres up to around 160 mAh/g [52], [53]. As described in 2.2, carbon materials can host Li ions in two structures: the ordered graphitic structure as in graphite, or the disordered amorphous structure as in hard carbon. The carbon fibre consists of both ordered and disordered domains. However, the ordered domain is not graphitic, but turbostratic, which obstructs the Li ions to properly intercalate between the graphene layers. The obstruction is more severe in the HM fibre with its big crystallites, and consequently the IM fibre performs better by hosting more lithium in the amorphous domain [44].

Lithiation, inserting lithium ions in the microstructure, affects the properties of the carbon fibre. During lithiation, the carbon fibre expands to fit the lithium ions. The axial and radial expansion is up to ~1% and ~5%, respectively. During delithiation, the carbon fibre contracts, but some volume change is irreversible, which is believed to be due to parts of the lithium being retained in the microstructure after delithiation [54]. Lithiation also affects the tensile strength of a carbon fibre, which is reduced by lithiation and partly regained by delithiation. Stiffness, however, is constant during lithiation [55], and capacity has proved to not be affected by tensile strain [56].

3 Experimental Method

This chapter explains the experimental work conducted to investigate the configuration of atoms and the atomic distribution in carbon fibres. First the investigated polyacrylonitrile (PAN) based carbon fibres are presented. Then the experimental methods of synchrotron hard X-ray photoelectron spectroscopy (HAXPES) and atom probe tomography (APT) are described. The general working principle of the techniques are explained and followed by detailing of the methodology performed by the author.

3.1 Materials

This thesis investigated three types of commercial PAN-based carbon fibres: M60J, T800, and IMS65. The three fibres were chosen since their electrochemical capacity and crystallite structure were known from previous studies [44], [52], [53]. M60J is a high modulus (HM) carbon fibre with large crystallites formed during graphitisation (Figure 3.1a), whereas T800 and IMS65 are intermediate (IM) fibres with more disordered carbon and smaller crystallites formed during carbonisation (Figure 3.1b-c). The ordered structure of M60J gives the HM fibre higher tensile modulus, higher thermal conductivity, and lower electrical resistivity than the IM fibre. On the other hand, the IM fibres have better tensile strength and electrochemical capacity. The physical and electrochemical properties of the fibres are summarised in Table 3.1.

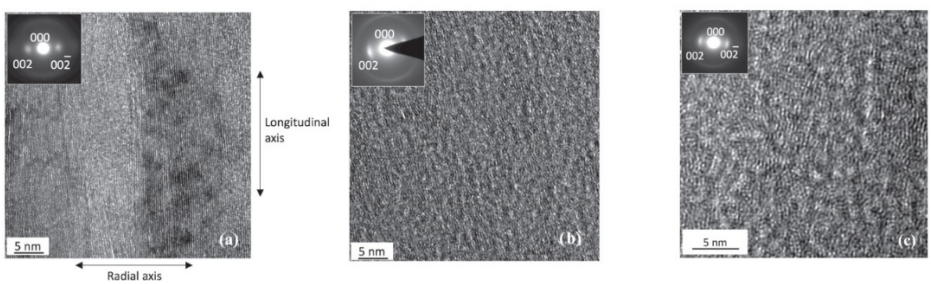

Figure 3.1: TEM micrographs of the microstructure of carbon fibres. a) The more ordered microstructure of M60J. b) The less ordered microstructure of IMS65 and c) T800. Adapted from Ref. [44] with permission from IOP Publishing.

Table 3.1: Physical properties, crystal structure and electrochemical performance of M60J, T800 and IMS65. Reproduced from Ref. [29]. CC BY 4.0.

	M60J	**T800**	**IMS65**
Final heat treatment temperature range (°C)	1800-3000	1100-1600	1100-1600
Tensile modulus (GPa)	588	294	290
Tensile strength (MPa)	3920	5490	6000
Electrical resistivity (Ω·cm $\times 10^{-3}$)	0.7	1.4	1.45
Thermal conductivity (cal/(cm·s·K))	0.363	0.0839	-
Average crystal length (Å)	>300	18	19
Average crystal thickness (Å)	>100	18	28
Interlayer spacing (002) (Å)	3.47	3.70	3.49
1st cycle capacity (mAh/g)	159	265	358
10th cycle capacity (mAh/g)	154	243	317

3.2 Synchrotron hard X-ray photoelectron spectroscopy

Synchrotron HAXPES is a non-destructive characterisation technique that can, similarly to conventional X-ray photoelectron spectroscopy (XPS), identify elemental composition and chemical states in materials, but with improved resolution, sensitivity, and increased analysis depth. Like XPS, HAXPES is also based on the photoelectric effect, where electrons are emitted when photons, such as X-rays, interact with a material. Analysis of the kinetic energy of the emitted electrons can reveal what atoms exist in the material and how they are bonded to surrounding atoms. For this thesis, the author used HAXPES on carbon fibres to determine the chemical states of atoms at varying depths.

3.2.1 Working principle of synchrotron HAXPES

In a synchrotron HAXPES experiment, high energy X-rays (so-called "hard" X-rays to distinguish them from low energy X-rays or "soft" X-rays of conventional XPS) are generated by a synchrotron light source. A synchrotron is a cyclic particle accelerator that, with strong magnetic fields, can bend the trajectory of electrons traveling at velocities near the speed of light into a closed loop. When the high-velocity electrons are forced to change direction in the magnetic field, they emit photons in the forward direction of the tangent. The resulting narrow cone of photons has high brilliance, high collimation, high flux, and wide energy tunability range, which gives HAXPES higher resolution and wider range of X-ray energies (~2000-15000 eV) than conventional XPS with sources of Mg K_α (1253.6 eV) or Al K_α (1486.6 eV) [57].

The underlying physics of HAXPES is the same as conventional XPS. The generated photons (X-rays) are directed towards the material to be investigated. The energy of an incident photon, E_{photon}, is absorbed by an electron within the material, and if the absorbed energy is greater than the electron's binding energy to its atom, $E_{binding}$, the residual energy will be converted to a kinetic energy, $E_{kinetic}$, with which the electron is ejected. The equation of the photoelectric effect, in which ϕ is the work function of the material, can be written:

$$E_{kinetic} = E_{photon} - (E_{binding} + \phi).$$

The binding energies of electrons are different for different elements and electron configurations. For example, in a carbon material, the binding energy of a 1s electron in a carbon atom (C1s) is ~285 eV, whereas in a nitrogen atom (N1s) the binding energy is ~400 eV. Since the instrument is equipped with a detector that counts electrons and registers their kinetic energy, and the photon energy is known from the X-ray source, an intensity spectra for binding energies can be generated and analysed.

The most apparent difference between HAXPES and XPS, is the increased probe depth of HAXPES. Typically, X-rays can travel longer distances in solids than electrons before interacting with matter and losing energy, i.e. the absorption length of X-rays is longer than the inelastic mean free path (IMFP) of electrons. Thus, IMFP is the depth limiting factor for information (electrons) to reach the detector. After a certain threshold, the IMFP increases with increased kinetic energy. HAXPES utilises much higher X-ray energies, and the consequently higher kinetic energies of the ejected electrons allow retrieval of deeper situated information. The information depth (ID) can be estimated with following expression:

$$\mathrm{ID} \approx \mathrm{IMFP} \times \ln\left(\frac{1}{1-(P/100)}\right),$$

where P is the percentage of detected electrons originating within the ID [58]. In other words, 95 % of the detected electrons originate within the depth of approximately three times the IMFP. With the tuneable X-ray energies of synchrotron HAXPES, different depths can be investigated.

X-ray energies also influence the photoionisation cross-section (the probability of a photon inducing ionisation of an atom and ejecting an electron). The

photoionisation cross-section decreases with increased energy of the incident X-ray. Thus, high-energy X-rays yield a less intense spectrum. This has historically prevented the use of hard X-rays in favour of soft X-rays, but with the high brightness of synchrotron light sources, this limitation has been overcome [57].

The photoionisation cross-section too is element dependant, which means that different elements have different probabilities to create photoelectrons, i.e. elements have different sensitivities. This must be considered for quantitative analysis of intensity spectra. Even though the peak intensities are related to the amounts of elements within the material, the relative peak intensities are skewed due to the difference in sensitivity. Besides photoionisation cross-sections, the peak intensities must also be corrected with instrument specific parameters. The so-called relative sensitivity factors are often used to compensate for photoionisation cross-sections and instrument specific parameters. Subsequently, the corrected peak intensity can be used to obtain quantitative atomic composition percentage values.

HAXPES can also determine the local bonding environment of an atom by detecting subtle shifts in the binding energies that depend on neighbouring atoms and bonding hybridisation. For instance, the binding energy of N1s in a nitrogen atom bonded to two carbon atoms in a graphene layer is ~398.5 eV, whereas it is ~401.0 eV in a nitrogen atom bonded to three carbon atoms in a graphene layer. However, even with the high resolution of synchrotron HAXPES, peaks close to each other can overlap. To determine the fraction of different chemical states the overlapping peaks are deconvoluted with software driven curve fitting tools.

3.2.2 HAXPES on carbon fibres

HAXPES was performed on the three types of carbon fibres M60J, T800, and IMS65. Even though HAXPES has some probing depth, it is still surface sensitive (the maximum analysis depth is ~40 nm in the present studies). Therefore, the sizing material on the M60J and T800 fibres had to be removed prior to the experiment. The sizing was removed by submerging fibre tows in acetone solvent in 50°C ultrasonic bath for an hour. IMS65 was received without sizing and was thus omitted from the acetone bath. Tows of all three fibre types were rinsed with isopropanol three times, and then, to vaporise residual liquid, placed in a Heraeus UT5050E oven for 3.5 hours in low vacuum condition of 40 mbar.

HAXPES was performed at the P22 undulator beamline at the synchrotron facility PETRA III (Deutsches Elektronen-Synchrotron, Hamburg) with capabilities of hard X-rays ranging from 2.4 to 15 keV [59]. Three X-ray energies were chosen to probe at different depths: 2.5, 4.6, and 7.2 keV. With these energy levels and the IMFP of graphitic materials approximated according to [60], 95% of the detected photoelectrons were estimated to originate within 17, 28, and 40 nm from the fibre surface for the respective X-ray energy. The projected beam size of 100 µm was many times larger than the fibre diameter of 5 µm, which means that multiple fibres were analysed simultaneously by the same beam.

Survey scans for binding energies of 0-600 eV revealed peaks at 285, 400, and 532 eV, associated to C1s, N1s, and O1s, respectively. Narrow scans at these three peaks were performed for increased resolution with various number of sweeps and dwell time: two 0.3 second sweeps at C1s, six 1 second sweeps at N1s, and four 0.5 second sweeps at O1s. The peak intensities were normalised to photoelectron counts per second. Shirley type background removal was performed using the software MultiPak 9.7.0.1. The photoionisation cross-section for C, N, and O at the three X-ray energies were calculated according to [61] (Table 3.2). The relative atomic composition X of element i was calculated by

$$X_i = \frac{\frac{I_i}{\left(\frac{d\sigma}{d\Omega}\right)_i}}{\frac{I_C}{\left(\frac{d\sigma}{d\Omega}\right)_C} + \frac{I_N}{\left(\frac{d\sigma}{d\Omega}\right)_N} + \frac{I_O}{\left(\frac{d\sigma}{d\Omega}\right)_O}},$$

where I is the background corrected normalised peak intensity and $(d\sigma/d\Omega)$ is the photoionisation cross-section.

The N1s peak at ~400 eV was desirable to deconvolute since the chemical states of N have previously proved to affect the electrochemical properties of carbon materials (see 2.2). Curve fitting with MultiPak 9.7.0.1 deconvoluted the N1s peak into five peaks at 398.5, 399.6, 401.0, 402.2, and 403.8 eV. These were respectively associated to pyridinic-N, pyrrolic-N, graphitic-N, edge-located graphitic-N, and oxidic-N (Figure 3.2).

After intensity corrections and peak deconvolutions, the data were analysed quantitatively. The relative atomic compositions of the carbon fibres were estimated at the three information depths, 17, 28, and 40 nm, to create a depth profile for each fibre type. The fractions of chemical states of N for each information depth were also estimated to reveal how the chemical states of N change with depth and differ in the carbon fibre types.

Table 3.2: Photoionisation cross-sections for C, O, and N at X-ray energies 2.5, 4.6, and 7.2 keV.

Element	X-ray energy (keV)	Photoionisation cross-section (10^{-21} cm^2)
C	2.5	4.141094016185717
	4.6	0.5587611167761363
	7.2	0.12926516381728224
O	2.5	12.887327483502218
	4.6	1.867057026381997
	7.2	0.450987214919451
N	2.5	7.681949384412015
	4.6	1.075128323988651
	7.2	0.25435714147955257

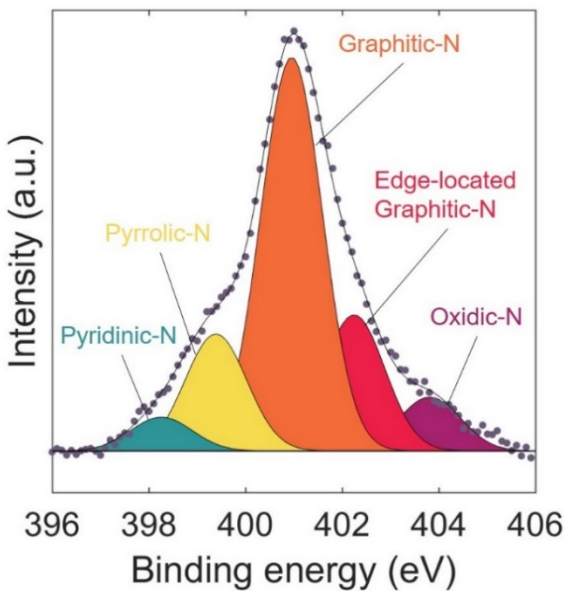

Figure 3.2: Deconvoluted N1s peak of IMS65 with five N species curve fitted: pyridinic-N, pyrrolic-N, graphitic-N, edge-located graphitic-N, and oxidic-N. Adapted from Ref. [29]. CC BY 4.0.

3.3 Atom Probe Tomography

APT is a microscopy technique that can compositionally quantify and visualise a tiny volume of a material atom-by-atom in three dimensions. APT is unique in its powerful combination of atomic scale spatial resolution (up to around 0.3 to 0.5 nm in lateral and 0.1 to 0.3 nm in depth direction) and high and equal sensitivity to all elements in the periodic table [62]. From the collected data on position coordinates and detected time of flight (which corresponds to mass-to-charge ratio), a three-dimensional representation of the original atomic distribution in the probed material is digitally reconstructed and analysed. In the work behind this thesis the author has developed the methodology for APT experiments on the traditionally challenging material of carbon fibres [63], [64] and been the first to present a three-dimensional atomic reconstruction of a carbon fibre. The following sections explain the working principle of APT and how APT experiments on carbon fibres are conducted.

3.3.1 Working principle of APT

APT is a destructive characterisation technique where atom-by-atom, a needle shaped specimen is field evaporated and registered (Figure 3.3). The evaporation relies on positive-ion emission by a very high electric field. To produce the field, a cryogenically cooled (≤100°K) and sharp specimen with tip radius <50 nm is subjected to either a voltage pulse or a laser pulse superimposed on a standing voltage of a few thousand volts. When the field is sufficiently strong, there is a good probability that the local bonding of the atoms to the specimen surface can be broken and the atom evaporated. Ideally, ions are only emitted during pulsing, and not between the pulses. The field required for the evaporation is contingent on the element and the surrounding atoms. Field evaporation happens selectively at the sharpest feature as that is where the local field is the highest. Thus, for APT tips with rough surfaces, field evaporation provides a final step of specimen preparation, by removing any protrusions, and forming an evenly rounded surface. As the evaporation process continues, the most protruding place on the tip is sequentially shifted to a new atom, and thereby the evaporation sequence can be approximated [62].

Before the advent of field evaporation aided by laser pulsing, voltage pulsing limited the use of APT to materials with electrical conductivity higher than 10^2 S/cm i.e. primarily metals [65]. It was not until recently that consensus view has been reached on the mechanisms by which laser pulsing induces ion emission. It is believed that the momentarily heating of the apex from the laser shifts the required field strength below the one created by the standing voltage

(Figure 3.4). Carbon fibres are good conductors, but susceptible to the high mechanical stresses induced by high voltages [66]. Thus, voltage pulsing can easily lead to premature failure of specimens and drastically limit the amount of data collected during an experiment run. Laser pulsing relieves the carbon fibre material of some of the high stresses, and therefore this thesis focuses on the laser-pulsed atom probe.

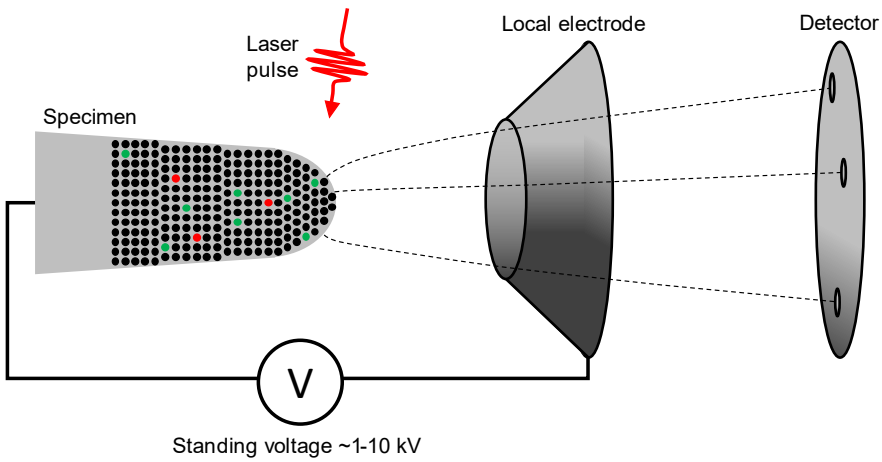

Figure 3.3: Schematic representation of a laser-pulsed local electrode atom probe.

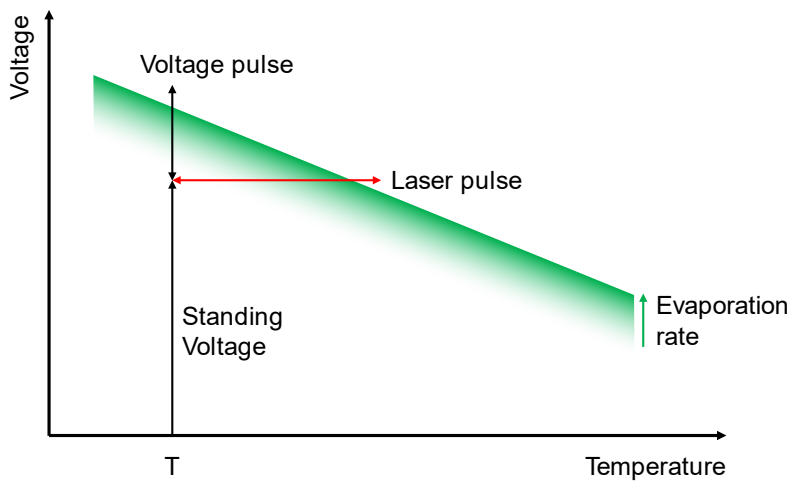

Figure 3.4: Schematic representation of the relation between specimen temperature, voltage, and evaporation rate.

Shortly after an ion has been evaporated by a pulse, it passes the local electrode and thereafter does not experience any field before hitting the detector, which records the time-of-flight (ToF) of the ion. Due to the conservation of energy, the potential energy of an ion exposed to an electric field is converted into kinetic energy when the atom is emitted and ionised. The potential energy is written as $E_{potential} = neV$, where n is the number of electrons removed from the atom (the charge state of the ion), e is the elementary charge, and V is the applied voltage. The kinetic energy is written as $E_{kinetic} = mv^2/2$, where m is the mass, and v is the velocity of the ion. The velocity is assumed to be constant, and thus $v = d/t$, where d is the distance between specimen tip and detector, and t is the ToF. In the combined energy equation, the mass and charge state of the detected ion can be calculated according to,

$$\frac{m}{n} = 2eV\frac{t^2}{d^2}.$$

The mass-to-charge ratio, m/n, is then used to identify the chemical species of the ion. For example, the mass-to-charge ratio of 12 Da is often assumed to be related to a carbon consisting of six protons and six neutrons with a charge state of 1+, $^{12}C^{1+}$. However, 12 Da can also be related to a magnesium ion consisting of twelve protons and twelve neutrons with a charge state of 2+, $^{24}Mg^{2+}$. How to differentiate overlapping mass-to-charge peaks is discussed in detail in 3.3.4.

The detector is position sensitive in two dimensions, and thus records the hit location in x- and y-coordinates. Based on the hit location and assumptions on the trajectory, the original position of the ions can be approximated. Progressively, atom after atom is removed from the surface, revealing the layer underneath. The hit sequence of ions along the specimen axis (z-coordinate) is recorded during the sequential evaporation of atoms layer after layer. With the combination of two-dimensional hit location and field evaporation sequence the three-dimensional image can be reconstructed [62].

3.3.2 Specimen preparation

The shape of the APT specimen has decisive effect on the success of the APT experiment. The needle shaped specimen is generally attained through either electropolishing by corroding away material in an electrolyte, or ion polishing by sputtering away material. The work behind this thesis utilised the later method in a dual beam FEI Versa 3D workstation, a combined focused ion-beam and scanning electron microscope (FIB/SEM). The ion column and the electron

column are at 52° angle relative to each other. The FIB uses a set of electrostatic lenses to focus the ion-beam from a gallium (Ga) liquid metal ion source. The energetic beam sputters away material by ion-bombardment, and the process can be monitored in real-time by the SEM equipped with detectors for secondary and backscattered electron imaging. The instrument can deposit platinum (Pt) on the target material by injecting Pt-containing gas and allowing the gas to interact under the scanning of either the electron-beam from the SEM or the ion-beam from the FIB. For micro-manipulation, the instrument is equipped with an Omniprobe system.

Before inserting the carbon fibre into the FIB/SEM, a stereomicroscope and a pincer were used to isolate individual fibres from a fibre bundle. The single fibre was placed on a small piece of silicon (Si) wafer and adhered at two points with a conductive silver glue. To accommodate specimen extraction from both the lateral surface and the cross-sectional surface of the carbon fibre, the mounting was performed in two ways. The wafer was adhered either horizontally to an aluminium stub for lateral extraction, or vertically with a free fibre end pointing upwards, sticking out from the wafer, for cross-sectional extraction.

A lift-out technique [67] was applied to prepare APT specimens (Figure 3.5). To protect the region of interest in the carbon fibre from Ga implantation during milling, a ~1 μm thick protective layer of Pt was applied through first electron-beam (2.0 kV and 4.0 nA) and then ion-beam (30 kV and 100 pA) induced chemical vapour deposition. The region of interest was 15×1.5 μm^2 for the lateral and 5×1.5 μm^2 for the cross-sectional extraction. The stage was tilted 22° and the ion-beam (30 kV and 3 nA) milled a coarse trench along the Pt layer and slightly longer than the layer, followed by gentler milling (30 kV and 1nA). The stage was rotated 180° and the milling repeated on the other side of the protective Pt layer. The stage was tilted 52° to be perpendicular to the ion-beam. The wedge of carbon fibre was cut on one end in the transverse direction, leaving the wedge just held at one end. The stage was then tilted back to 0°. The needle of the Omniprobe was inserted and attached by Pt deposition to the free end of the wedge. A final small trench was milled at the other end of the wedge to separate it from the rest of the carbon fibre. The stage was lowered and a coupon with pre-manufactured micro-posts of Si (CAMECA) was inserted in the FIB/SEM. The end of the wedge of carbon fibre material was placed on a micro-post, adhered with Pt deposition on one side, cut away from the rest. The process was repeated until the wedge had been consumed, yielding material for 2-5 posts for each lift-out. It should be noted that cross-sectional extraction is

limited by the fibre diameter, whereas the yield of lateral extraction is higher per lift-out. Then, the stage was rotated 180°, and adhered with Pt on the other side.

The final step was to mill the material piece into a sharp APT specimen. It was done through a series of annular milling. For the initial milling the acceleration voltage was 30 kV, the ion current was 500 pA, the outer diameter of the milling pattern was 3 µm, and the inner diameter was 2 µm. Then the ion current and the inner diameter were gradually decreased to 100 pA and 0.15 µm, and final polishing at acceleration voltage at 2 kV and ion current 27 pA (Table 3.3).

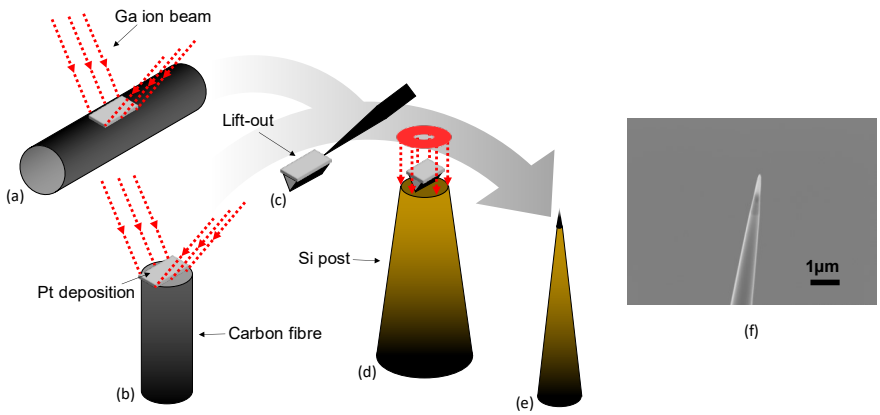

Figure 3.5: Schematic of carbon fibre specimen fabrication for APT. A protective Pt layer is deposited on (a) the lateral or (b) the cross-sectional fibre surface; and the Ga ion beam mills a wedge shape close to the Pt layer. (c) The wedge of carbon fibre is cut free and extracted using the micro-manipulator. (d) Part of the wedge is adhered with Pt to a Si post, cut free, and annularly milled to (e) a sharp tip. (f) A SEM image of a sharpened APT tip of carbon fibre. Reproduced from Ref. [29]. CC BY 4.0.

Table 3.3: Settings for FIB milling and polishing for APT specimen preparation.

Inner diameter (µm)	Ion current (pA)	Acceleration voltage (kV)
2.0	500	30
1.5	500	30
1.0	300	30
0.8	300	30
0.5	100	30
0.3	100	30
0.2	100	30
0.15	100	30
0	48	5
0	27	2

3.3.3 Data Collection

An IMAGO LEAP 3000X HR in pulsed laser mode was used to conduct APT analyses. It is equipped with a diode-pumped neodymium-doped yttrium orthovanadate (Nd:YVO_4) solid state laser. The wavelength is 532 nm and laser pulse duration is 12 ps. The specimen temperature was set to 100 K. The acquisition rate was set to 2 ions per 1000 pulses (0.2%). The detector efficiency was 37 % and image compression factor was 1.65.

During APT experiments, premature specimen fracture is a common challenge caused by high mechanical stresses induced by the high electric field [66]. Through trial-and-error, it was concluded that the experiment run length was longest when the laser energy was set to 1 nJ and the laser pulse frequency was set to 100 kHz. Around 40 specimens were run, but less than half yielded useful results.

In order to achieve long runs, the standing voltage must be increased carefully. Firstly, the voltage was raised to and held at around 800 V, while the laser scanned over the tip to find the apex and thus initiate the field evaporation. Typically, no field evaporation occurred at 800 V, and if it did, only short bursts of residual Ga or Pt were detected. From 800 V the voltage was raised in regular intervals of 200 V with a laser scan between each voltage rise. The initiation voltage for continuous field evaporation was normally found after 2500 V, but for some instances a run might not initiate until 5000 V. The different initiation voltages were attributed to the variation in sharpness of the specimen tips, with the sharper specimen initiating at the lower voltage.

When continuous field evaporation was established, the voltage control was set to “automatic”: the standing voltage was adjusted automatically according to the real evaporation rate. Initially, laser scanning was also set to automatic, i.e. for a set time interval, the laser scans in a small area to ensure that it remains at the very tip of specimen. However, automatic laser scanning was proved to disrupt the field evaporation, and consecutive automatic attempts to regain field evaporation often led to specimen fracture. Thus, no automatic laser scanning was used. The voltage history curve exhibited a jagged appearance (Figure 3.6) since occasional bursts of evaporating ions pushed the field evaporation above the set limit of 2 ions per 1000 pulses, and the instrument responded with decreasing the standing voltage until the set evaporation rate was regained. It turned out that acquiring more than 1 million ions was challenging, which only four experiment runs managed. The maximum number of ions acquired during

one run was 4.13 million. Generally, the runs with lower initiation voltage (i.e. sharper specimens) ran longer.

For data interpretation it is important to have high mass resolution, i.e. thin peaks in the mass-to-charge spectra. The width of the peaks heavily depend on variations in the measured ToF. The ToF is approximated by measuring the time from the laser pulse until an ion hit is detected by the detector. If an ion evaporation is delayed relative the laser pulse, its measured ToF will be larger. Delayed evaporation can occur because of residual heat that is not properly dissipated from the apex of the APT tip, and manifests as so-called thermal tails in the mass spectra and broadens the peaks. Thus, good heat dissipation is required for high mass resolution. Three strategies were employed for improving the heat dissipation in the APT tips. The mass resolving power was evaluated by comparing the full width at half maximum (FWHM) for the 12 Da peak.

- Blunter APT tips were manufactured, since they have a larger cross-section and hence can conduct heat more quickly. This proved to be very effective for improving resolution as the resolving power of the sharpest T800 specimen was ~80, and for the bluntest was ~570 (Figure 3.7a). However, blunt tips create weaker local electric fields, which requires the voltage to be higher to initiate and maintain evaporation. The high voltage induces high mechanical stresses, and the possibility of premature fracture is increased, which leads to shorter experiment runs with less acquired ions. Thus, there is a trade-off between the mass resolution and the size of the acquired data.
- The laser pulse frequency was reduced from 200 to 100 kHz. This increased the mass resolving power of M60J from ~310 to ~850 (Figure 3.7b). Between laser pulses, the tip needs time to cool down to the base temperature or else it risks accumulating heat at the next pulse and generating delayed evaporation. With decreased frequency, the cooling time between pulses was extended and the residual heat had more time to dissipate.
- APT tips were prepared from material extracted from the cross-section of the carbon fibres rather than using lateral specimens. Since the microstructure of a carbon fibre is anisotropic, with graphene layers in the crystallites aligned in the fibre direction, its thermal conductivity is better in the fibre direction. The mass resolving power was improved from ~250 for lateral specimens to ~580 for cross-sectional specimens

of T800 (Figure 3.7c). Nevertheless, for cross-sectional specimens, the amount of material per lift-out operation is limited by the diameter of the carbon fibre, and the specimen preparation is more challenging and time consuming.

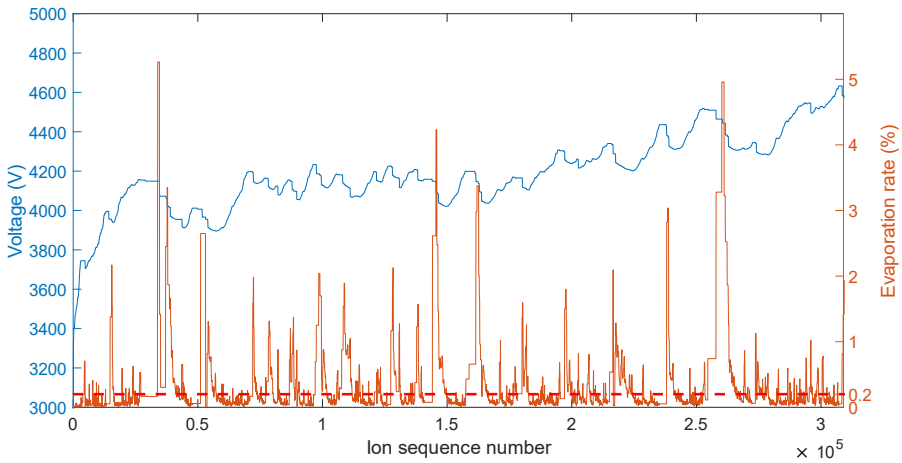

Figure 3.6: Voltage history of an APT experiment run with corresponding evaporation rate history.

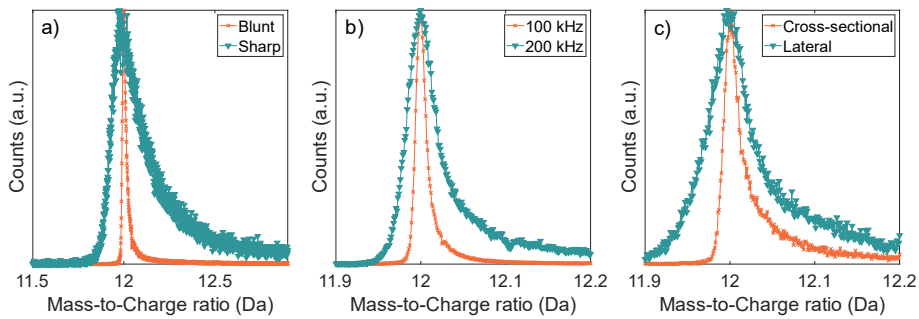

Figure 3.7: Factors that influence mass resolution. Only normalized 12 Da peaks are shown and used to compare the resolution. (a) Mass spectra of a blunt and a sharp specimen tip at 12 Da. The blunt specimen leads to better resolution. (b) Mass spectra at pulse frequency of 100 and 200 kHz. 100 kHz leads to better resolution. (c) Mass spectra of cross-sectional and lateral specimens. The cross-sectional geometry leads to better resolution.

3.3.4 Data interpretation

Carbon fibres consist of C, N, and O, but the mass-to-charge spectra of carbon fibres were complex with near one hundred mass-to-charge peaks (Figure 3.8). Assigning these peaks to associated ions was a big challenge, but was easier for the HM fibres M60J, since its high final heat treatment temperature had expelled many of the non-carbon atoms and made the fibre chemically simpler than IM fibres. Additionally, the higher thermal conductivity of M60J allowed for higher mass resolution. The peak assignment of HM fibres was therefore used as a guide for assignment of peaks in the more complex spectra of IM fibres.

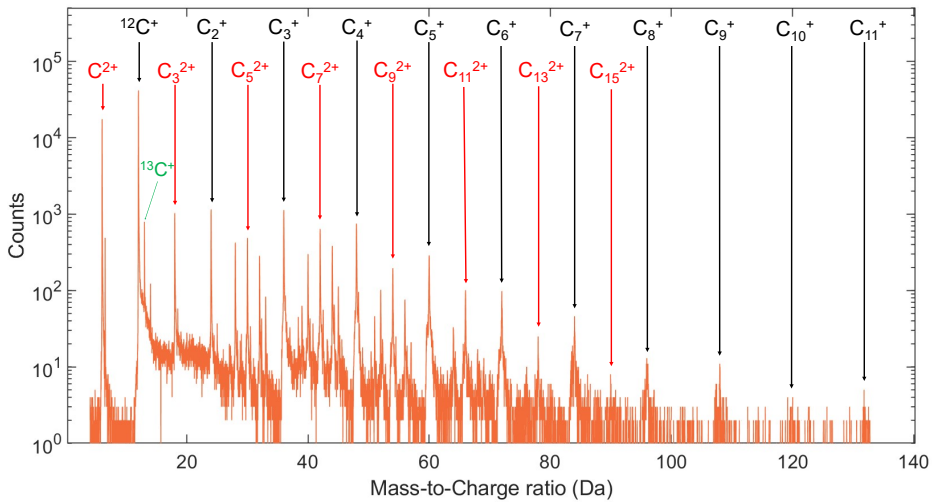

Figure 3.8: A mass spectrum of M60J. Peaks associated with pure carbon ions of charge state 1+ and 2+ are marked.

Given that C is the most predominant element in carbon fibres, it was convenient to start identifying peaks consisting of only carbon ions. Carbon has two stable isotopes: ^{12}C and ^{13}C, with the latter containing one more neutron than the former. Naturally found on Earth, 98.93% of carbon atoms are carbon-12 and 1.07% are carbon-13. During an APT analysis on carbon fibres, n charged cluster ions containing x carbon atoms, C_x^{n+}, can be evaporated. These cluster ions can contain both type of isotopes, but statistically it is most likely that they either contain only carbon-12, $^{12}C_x^{n+}$, or one carbon-13 and the rest being carbon-12, $^{12}C_{(x-1)}{}^{13}C^{n+}$ (Figure 3.9). APT can distinguish the two isotopes, which are expressed in the mass-to-charge spectra as a main peak for the more common $^{12}C_x^{n+}$ and a minor satellite peak for the rarer $^{12}C_{(x-1)}{}^{13}C^{n+}$. The majority of mass-to-charge peaks were identified by systematically searching for carbon

cluster ions with x=1 to 22 and n=1 to 5. In Table 3.4, mass-to-charge ratios marked in green are confirmed in the mass spectra of M60J.

However, multiple of the main peaks can overlap. For example, the peak at 36 Da can consist of $^{12}C_3^+$, $^{12}C_6^{2+}$, $^{12}C_9^{3+}$, and $^{12}C_{12}^{4+}$. Fortunately, satellite peaks do not overlap. For example, the satellite peaks of $^{12}C_2{}^{13}C^+$, $^{12}C_5{}^{13}C^{2+}$, $^{12}C_8{}^{13}C^{3+}$, and $^{12}C_{11}{}^{13}C^{4+}$ have mass-to-charge ratio of 37, 36.5, 36.33, and 36.25, respectively. Thus, the satellite peaks can be used to deconvolute the overlapping main peaks. Based on the probability to find $^{12}C_x^{n+}$ or $^{12}C_{(x-1)}{}^{13}C^{n+}$, a theoretical ratio, R, between satellite and main peak can be calculated by

$$R = \frac{x(0.0107 \times 0.9893^{x-1})}{0.9893^{x}}.$$

The size of a main peak without overlap will comply with the theoretical ratio with respect to the size of its satellite peak. On the other hand, a peak consisting of overlapping main peaks is deconvoluted by estimating the size of the individual peaks based on the size of their respective satellite peak and the theoretical ratio (Figure 3.10). For this kind of analysis, it is important with high mass resolution and large numbers of acquired ions to clearly distinguish the small satellite peaks.

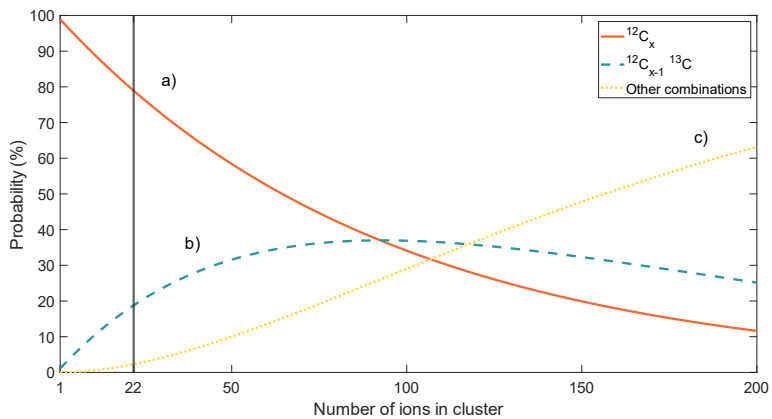

Figure 3.9: The probability of a cluster ion consisting of a) only carbon-12, b) one carbon-13 and the rest carbon-12, and c) other combination of carbon-12 and carbon-13. Note that the largest cluster ion encountered was C_{22}^{5+}, and for such small cluster ions the probability of other combinations is relatively low.

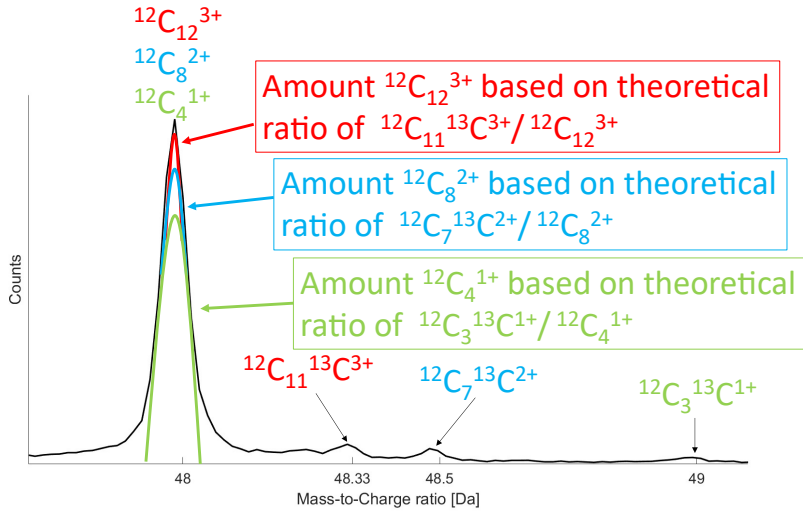

Figure 3.10: Small range of a mass spectrum around 48 Da. There are satellite peaks at 48.33, 48.5 and 49 Da corresponding to $^{12}C_3{}^{13}C^{1+}$, $^{12}C_7{}^{13}C^{2+}$ and $^{12}C_{11}{}^{13}C^{3+}$, thus the main peak at 48 Da consists of overlapped peaks $^{12}C_4{}^{1+}$, $^{12}C_8{}^{2+}$ and $^{12}C_{12}{}^{3+}$. The green peak is the deconvoluted $^{12}C_4{}^{1+}$ peak, the blue $^{12}C_8{}^{2+}$, and the red $^{12}C_{12}{}^{3+}$. The theoretical ratio is based on the natural abundance of ^{12}C and ^{13}C, 98.93% and 1.07%, respectively. Reproduced from Ref. [29]. CC BY 4.0.

The theoretical ratio between satellite and main peak can also be used to identify whether pure carbon peaks overlap with peaks consisting of other elements. For M60J, the satellite-to-main peak ratio for $C_7{}^{3+}$ and $C_{11}{}^{3+}$ did not match the theoretical ratio. Thus, the peaks at 28 Da and 44 Da were assigned to also consist of CO^+ and $CO_2{}^+$, and were deconvoluted based on the size of the satellite peaks.

Another reason for using the theoretical ratio and satellite peaks to evaluate the main peaks, is the dead time of the detector. When ions reach the detector within close proximity in space and time, the detector can fail to register every and each ion. Since the main peaks consist of more ions than the satellite peaks, main peak ions reach the detector more frequently than satellite peak ions, and thus the effect of the detector dead time is more severe for main peak ions. Consequently, in the mass spectra, the main peaks are underestimated, whereas the satellite peaks are nearer the true ion count and can be used to correct the ion count in the main peak towards a more accurate value [68].

After the systematic identification of pure carbon ions and their overlaps in the mass spectra of M60J, only one small unidentified peak remained: 14 Da. The

peak can correspond to N^+ or CO^{2+}. However, since no other peak associated with nitrogen was observed, it was assumed that the peak consisted of CO^{2+}, with reservations about trace amounts of N^+.

In the mass spectra of the IM fibres T800 and IMS65, the 14 Da peak was much larger, which was attributed to higher nitrogen contents, and the peak was assigned to mostly consist of N^+. The T800 and IMS65 mass spectra included the same peaks as the M60J spectra, but also peaks at 7, 19, 26, 27, 28.67, 31, 32.67, 36.67, 38, 40.67, 43, 44.67, 50, 55, 62, 67, 74, 86 Da. These were assigned as C_xN^{n+} and C_xNO^{n+} (Table 3.5).

With the spectra of the three types of carbon fibres completely characterised, the three-dimensional digital reconstruction was the last step. The tip radius and shank angle of the reconstruction volumes were estimated by measuring SEM images of specimen tips, and the software IVAS 3.4.3 was used to create the first ever published 3D reconstruction of atom map for carbon fibres (Figure 3.11). Atomic composition was calculated by translating the ion count in each peak to atom counts, i.e. one C_2NO^{2+} ion in the 27 Da peak was translated to two C atoms, one N atom, and one O atom. With the 3D reconstructions, the distribution patterns of atoms were possible to investigate.

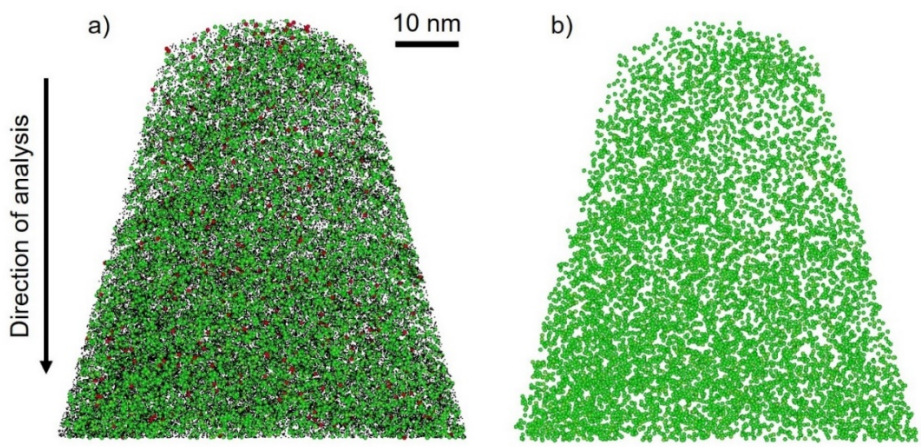

Figure 3.11: 3D atom-by-atom reconstructions of T800 showing a) C, N, and O, and b) only N. C-related ions are represented by black dots, N-related ions by green bubbles, and O-related ions by red bubbles. For the sake of clarity, only 5% C-related ions, 10% N-related ions and 10% O-related ions are shown.

Table 3.4: Mass-to-charge ratio for pure C ions at different charge states with corresponding main (M) and satellite (S) peaks, $^{12}C_x^{n+}$ and $^{12}C_{(x-1)}{}^{13}C^{n+}$, respectively. The mass-to-charge ratios marked in green were confirmed in the mass spectra of M60J, either by uniqueness of the ratio or the corresponding satellite peak; and the ratios marked in orange lack confirmation by the satellite peak, which may be overshadowed by the tail of the major peak, or be too small to be distinguished with certainty. The last column lists theoretical ratio between the satellite and main peak (S/M) based on natural abundance of carbon isotopes.

	Charge state 1+		**Charge state 2+**		**Charge state 3+**		**Charge state 4+**		**Charge state 5+**		
	M	**S**	**M**	**S**	**M**	**S**	**M**	**S**	**M**	**S**	**S/M**
C_1	12	13	6	6.5	4	4.33	3	3.25	2.4	2.6	1.08%
C_2	24	25	12	12.5	8	8.33	6	6.25	4.8	5	2.16%
C_3	36	37	18	18.5	12	12.33	9	9.25	7.2	7.4	3.24%
C_4	48	49	24	24.5	16	16.33	12	12.25	9.6	9.8	4.33%
C_5	60	61	30	30.5	20	20.33	15	15.25	12	12.2	5.41%
C_6	72	73	36	36.5	24	24.33	18	18.25	14.4	14.6	6.49%
C_7	84	85	42	42.5	28	28.33	21	21.25	16.8	17	7.57%
C_8	96	97	48	48.5	32	32.33	24	24.25	19.2	19.4	8.65%
C_9	108	109	54	54.5	36	36.33	27	27.25	21.6	21.8	9.73%
C_{10}	120	121	60	60.5	40	40.33	30	30.25	24	24.2	10.82%
C_{11}	132	133	66	66.5	44	44.33	33	33.25	26.4	26.6	11.90%
C_{12}	144	145	72	72.5	48	48.33	36	36.25	28.8	29	12.98%
C_{13}	156	157	78	78.5	52	52.33	39	39.25	31.2	31.4	14.06%
C_{14}	168	169	84	84.5	56	56.33	42	42.25	33.6	33.8	15.14%
C_{15}	180	181	90	90.5	60	60.33	45	45.25	36	36.2	16.22%
C_{16}	192	193	96	96.5	64	64.33	48	48.25	38.4	38.6	17.31%
C_{17}	204	205	102	102.5	68	68.33	51	51.25	40.8	41	18.39%
C_{18}	216	217	108	108.5	72	72.33	54	54.25	43.2	43.4	19.47%
C_{19}	228	229	114	114.5	76	76.33	57	57.25	45.6	45.8	20.55%
C_{20}	240	241	120	120.5	80	80.33	60	60.25	48	48.2	21.63%
C_{21}	252	253	126	126.5	84	84.33	63	63.25	50.4	50.6	22.71%
C_{22}	264	265	132	132.5	88	88.33	66	66.25	52.8	53	23.79%

Table 3.5: Mass-to-charge-ratio of N containing ions at different charge states. Peaks marked in green were confirmed in the mass spectra of IM fibres, and peaks in orange may exist, but could not be confirmed due to overlap with other peaks.

	Charge state 1+	Charge state 2+	Charge state 3+
N	14	7	4.67
CN	26	13	8.67
C_2N	38	19	12.67
C_3N	50	25	16.67
C_4N	62	31	20.67
C_5N	74	37	24.67
C_6N	86	43	28.67
C_7N	98	49	32.67
C_8N	110	55	36.67
C_9N	122	61	40.67
$C_{10}N$	134	67	44.67
C_2NO	54	27	18

4 Summary of appended papers

This chapter summarises the content and implications of the appended papers. **Paper I** deals with the methodology of performing atom probe tomography (APT) on carbon fibres, and thus lays the groundwork for **Paper II**, which focuses on elucidating structure-property relations in carbon fibres with synchrotron hard X-ray photoelectron spectroscopy (HAXPES) and APT.

Paper I proposes best practices for APT analysis on carbon fibres. Previously, few attempts of APT on carbon fibres were made, and information on how to perform experiments is scarce. **Paper I** discusses strategies for accurate measurement: how to assign peaks in the obtained mass spectra, how to improve mass resolution, how to deconvolute peaks with overlap, and how to reduce multiple hit events (see 3.3). The conclusion of **Paper I** is that APT on carbon fibres, although challenging, is possible with the help of the strategies presented. Since so little information has been available before, this is the first guide for APT on carbon fibres, and thus, it opens up research opportunities to gain further knowledge on carbon fibres and other carbon materials using the powerful technique of APT.

Paper II utilises HAXPES and APT to study the configuration and distribution of N heteroatoms in intermediate modulus (IM) and high modulus (HM) carbon fibres. N heteroatoms in carbon fibres are interesting to investigate since N is an inherent constituent of many carbon fibres, and N-doping has proved to enhance the electrochemical performance of other carbon materials (see 2.2). Still, the effect of this inherent N-doping on electrochemical properties of carbon fibres was not investigated before.

Previously, the higher capacity of IM fibres compared to HM fibres was attributed to smaller crystallites in IM fibres (see 2.4.3). **Paper II** presents further differences between IM and HM fibres, where the N content is distinctly higher in the IM fibres. It is recognised that the high final heat treatment temperature in manufacturing of HM fibres leads to less heteroatoms and larger crystallites (see 2.4.1). The higher N content and smaller crystallites can both contribute to the higher capacity of the IM fibres.

However, even within the category of IM fibre types, the capacity differs quite substantially. T800 has a capacity of 265 mAh/g compared to 358 mAh/g for IMS65. The crystallite size in the two IM fibres is similar and cannot explain the discrepancies in capacity. Furthermore, HAXPES and APT results show that the N contents in T800 and IMS65 are similar. What differentiates the two fibre types is the chemical states of N heteroatoms. It is found that IMS65 has a larger fraction of defect-creating N, i.e. pyridinic-N and pyrrolic-N. These defects are believed to work as active sites for insertion of Li-ions and boost the electrochemical performance of IMS65. Additionally, HAXPES demonstrates that the chemical states of N vary with depth in the carbon fibre, and APT reveals that N does not agglomerate and is evenly distributed on the short range but varies on the long range. Thus, it can be assumed that the electrochemical properties vary throughout a carbon fibre. The results from **Paper II** indicate that N heteroatoms play an important role in the electrochemical performance of carbon fibres, and that they can be used as a design parameter for multifunctional carbon fibres.

5 Future work

The work presented in this thesis is only a first step towards a fundamental understanding of the links between the microstructure of carbon fibres and their mechanical-electrochemical multifunctionality. A plethora of exciting research ventures still remains. In this chapter, possible future work is discussed.

APT and TEM of lithiated carbon fibres
So far, the work presented in this thesis has been focused on virgin carbon fibres, but tests on lithiated carbon fibres are still lacking. Future research will study the lithiated carbon fibres to truly bring understanding of where Li atoms are inserted. Furthermore, delithiated carbon fibres will also be investigated to reveal whether permanent changes are induced by lithiation; and if so, where Li are trapped in the microstructure. The most prominent foreseeable challenge to achieve this is the practical problem of transferring lithiated carbon fibres between instruments while avoiding reaction of the highly reactive Li with the atmosphere.

To understand the distribution of Li in carbon fibres under electrochemical cycles, the most obvious experiments that build on this thesis are atom probe tomography (APT) on lithiated and delithiated carbon fibres to map the local 3D distribution of Li. Through such experiments, it can be determined how Li is positioned, relative to other Li atoms and heteroatoms like N. Furthermore, transmission electron microscopy (TEM) and electron energy loss spectroscopy (EELS) on lithiated carbon fibres can reveal the distribution of Li at a larger scale, and answer the question of which domain, crystalline or amorphous, Li atoms preferably insert in.

Single filament tensile testing of lithiated carbon fibres
Previous mechanical tensile tests of lithiated carbon fibres were performed on fibre bundles consisting of thousands of fibres. The large number of fibres simultaneously loaded in a bundle test muddles the properties into an averaged value and gives rise to uncertainties regarding contribution of individual fibres. Nevertheless, these tests concluded that lithiation had little effect on tensile modulus but impaired the tensile strength. Still, the mechanisms behind this behaviour is not understood. Single filament tensile tests of individual lithiated and delithiated carbon fibres can elucidate the effect of lithiation on the

mechanical properties of carbon fibres. Future work will focus on a combination of tensile tests of individual fibres and in-situ scanning electron microscopy (SEM) observation of fracture processes, for correlation between mechanical properties and microstructure. SEM investigation of the fracture surfaces of broken fibres can provide answers to why lithiation impairs the tensile strength of carbon fibres. With the test rig inserted in the SEM instrument, real-time monitoring of the fracture moment can show the potential differences between virgin, lithiated, and delithiated carbon fibres under the fracture process. To control where along the fibre fracture will happen, and ensure that the SEM captures the course of fracture, milling with focused ion beam (FIB) will be used to introduce notches in the fibre and thus control where the largest stress concentration is located.

In-situ and operando observation of carbon fibre electrode

The above-mentioned experiments are all ex-situ in terms of electrochemical processes, meaning that the lithiation/delithiation takes place outside the experiments, i.e. SEM observations. However, in-situ testing is important for increased understanding of the dynamic electrochemical processes. This can be done by constructing an in-situ platform inside a FIB/SEM, that is equipped with a micro-manipulator which can be connected to a potentiostat. An in-situ half battery cell, with a carbon fibre electrode and compatible with the FIB/SEM, will undergo electrochemical cycles. The SEM monitors the lithiation and delithiation processes on the carbon fibre surface. Through serial milling by the FIB, layers of carbon fibre material can be removed. By combining consecutive 2D images, 3D information of the fibres can be obtained.

Manufacture of prototype carbon fibres

Finally, based on the knowledge gained from the above research, prototype carbon fibres can be designed, manufactured, and tested. This would remarkably increase the understanding of the relationship between manufacturing parameters, microstructure, and multifunctionality, especially given the detailed manufacturing processes behind commercial carbon fibres are largely unknown. Furthermore, the many small differences between commercial carbon fibre types, even within the same category, makes it difficult to derive causal relationship with full certainty. Instead, testing of prototype carbon fibres with only one process parameter differentiating them, gives a much clearer view. For example, to further understand the effect of N heteroatoms on the electrochemical performance, carbon fibres can be manufactured with different denitrogenation times and then be tested.

References

[1] Tesla, “Tesla Model S Owner’s Manual, Version 2018.48.12,” 2020. [Online]. Available: https://www.tesla.com/sites/default/files/model_s_owners_manual_north_america_en_us.pdf. (Accessed April 2021)

[2] BMW, “BMW i3.” [Online]. Available: http://www.bmw.com/. (Accessed April 2021)

[3] European Automotive Research Partners Association, “EARPA Position Paper Application driven material development & associated manufacturing processes,” 2013.

[4] European Commision, “Fligthphath 2050 Europe’s vision for aviation,” 2011.

[5] L. E. Asp, M. Johansson, G. Lindbergh, J. Xu, and D. Zenkert, “Structural battery composites: a review,” *Funct. Compos. Struct.*, vol. 1, no. 4, 2019.

[6] W. Johannisson, D. Zenkert, and G. Lindbergh, “Model of a structural battery and its potential for system level mass savings,” *Multifunct. Mater.*, vol. 2, no. 3, 2019.

[7] W. Johnson, “Structure of High Modulus Carbon Fibres,” *Nature*, vol. 215, pp. 384–396, 1967.

[8] M. Guigon and A. Oberlin, “Microtexture and Structure of Some High-Modulus , PAN-Base Carbon Fibres,” *Fibre Sci. Technol.*, vol. 20, pp. 177–198, 1984.

[9] M. Guigon and A. Oberlin, “Microtexture and Structure of Some High Tensile Strength , PAN-Base Carbon Fibres,” *Fibre Sci. Technol.*, vol. 20, pp. 55–72, 1984.

[10] M. Guigon and A. Oberlin, “Heat-treatment of high tensile strength PAN-based carbon fibres: Microtexture, structure and mechanical properties,” *Compos. Sci. Technol.*, vol. 27, no. 1, pp. 1–23, 1986.

[11] M. G. Northolt, L. H. Veldhuizen, and H. Jansen, “Tensile deformation of carbon fibers and the relationship with the modulus for shear between the basal planes,” *Carbon N. Y.*, vol. 29, no. 8, pp. 1267–1279,

1991.

[12] L. P. Kobets and I. S. Deev, “Carbon fibres: structure and mechanical properties,” *Compos. Sci. Technol.*, vol. 57, pp. 1571–1580, 1997.

[13] O. Paris, D. Loidl, H. Peterlik, H. Lichtenegger, and P. Fratzl, “The internal structure of single carbon fibers determined by simultaneous small- and wide-angle X-ray scattering,” *J. Appl. Crystallogr.*, vol. 33, pp. 695–699, 2000.

[14] M. Ji, C. Wang, Y. Bai, M. Yu, and Y. Wang, “Comparison of tensile fracture morphologies among various polyacrylonitrile-based carbon fibers,” *Polym. Bull.*, vol. 390, pp. 381–389, 2007.

[15] F. Liu, H. Wang, L. Xue, L. Fan, and Z. Zhu, “Effect of microstructure on the mechanical properties of PAN-based carbon fibers during high-temperature graphitization,” *J. Mater. Sci.*, vol. 43, pp. 4316–4322, 2008.

[16] F. Yang *et al.*, “Effect of amorphous carbon on the tensile behavior of polyacrylonitrile (PAN) -based carbon fibers,” *J. Mater. Sci.*, vol. 54, no. 11, pp. 8800–8813, 2019.

[17] B. D. Agarwal, L. J. Broutman, and K. Chandrashekhara, *Analysis and performance of fiber composites*, 4th ed. John Wiley & Sons, Inc., 2018.

[18] H. Berg, *Batteries for Electric Vehicles: Materials and Electrochemistry*. Cambridge University Press, 2015.

[19] A. J. R. Dahn *et al.*, “Mechanisms for Lithium Insertion in Carbonaceous Materials Mechanisms for Lithium Insertion in Carbonaceous Materials,” *Science (80-.).*, vol. 270, no. 5236, pp. 590–593, 1995.

[20] M. Inagaki, M. Toyoda, Y. Soneda, and T. Morishita, “Nitrogen-doped carbon materials,” *Carbon N. Y.*, vol. 132, pp. 104–140, 2018.

[21] A. L. M. Reddy, A. Srivastava, S. R. Gowda, H. Gullapalli, M. Dubey, and P. M. Ajayan, “Synthesis of nitrogen-doped graphene films for lithium battery application,” *ACS Nano*, vol. 4, no. 11, pp. 6337–6342, 2010.

[22] P. Han *et al.*, “Nitrogen-doping of chemically reduced mesocarbon microbead oxide for the improved performance of lithium ion batteries,” *Carbon N. Y.*, vol. 50, no. 3, pp. 1355–1362, 2012.

[23] T. Schiros *et al.*, “Connecting dopant bond type with electronic structure in n-doped graphene,” *Nano Lett.*, vol. 12, no. 8, pp. 4025–4031, 2012.

[24] D. Usachov *et al.*, “The chemistry of imperfections in N-graphene,” *Nano Lett.*, vol. 14, no. 9, pp. 4982–4988, 2014.

[25] X. Wang *et al.*, “Atomistic origins of high rate capability and capacity of N-doped graphene for lithium storage,” *Nano Lett.*, vol. 14, no. 3, pp. 1164–1171, 2014.

[26] F. Zheng, Y. Yang, and Q. Chen, “High lithium anodic performance of highly nitrogen-doped porous carbon prepared from a metal-organic framework,” *Nat. Commun.*, vol. 5, no. May, pp. 1–10, 2014.

[27] B. Zhang *et al.*, “Correlation between atomic structure and electrochemical performance of anodes made from electrospun carbon nanofiber films,” *Adv. Energy Mater.*, vol. 4, no. 7, 2014.

[28] Z. He *et al.*, “Electrospun nitrogen-doped carbon nanofiber as negative electrode for vanadium redox flow battery,” *Appl. Surf. Sci.*, vol. 469, no. September 2018, pp. 423–430, 2019.

[29] M. Johansen, C. Schlueter, P. Lam, L. E. Asp, and F. Liu, “Mapping nitrogen heteroatoms in carbon fibres using atom probe tomography and photoelectron spectroscopy,” *Carbon N. Y.*, vol. 179, pp. 20–27, 2021.

[30] E. L. Wong, D. M. Baechle, K. Xu, R. H. Carter, J. F. Snyder, and E. D. Wetzel, “Design and Processing of Structural Composite Batteries,” *Proc. Soc. Adv. Mater. Process Eng.*, 2007.

[31] P. Liu, E. Sherman, and A. Jacobsen, “Design and fabrication of multifunctional structural batteries,” *Journalof Power Sources*, vol. 189, pp. 646–650, 2009.

[32] L. E. Asp *et al.*, “A Structural Battery and its Multifunctional Performance,” *Adv. Energy Sustain. Res.*, vol. 2000093, 2021.

[33] S. K. Martha, N. J. Dudney, J. O. Kiggans, and J. Nanda, “Electrochemical Stability of Carbon Fibers Compared to Aluminum as Current Collectors for Lithium-Ion Batteries,” *J. Electrochem. Soc.*, vol. 159, no. 10, pp. 1652–1658, 2012.

[34] M. Sauer, “Composites Market Report 2019,” 2019.

[35] S. Park, *Carbon Fibers*, 2nd ed. Springer Nature, 2018.

[36] E. Fitzer, K.-H. Kochling, H. P. Boehm, and H. Marsh, "(IUPAC Recommendations 1995) Recommended terminology for description of carbon as a solid," *Pure Appl. Chem.*, vol. 67, no. 3, pp. 473–506, 1995.

[37] J.-B. Donnet, T. W. Wang, S. Rebouillat, and J. C. M. Peng, *Carbon fibres*, 3rd ed. Marcel Dekker Inc., 1998.

[38] E. Frank, L. M. Steudle, D. Ingildeev, J. M. Spçrl, and M. R. Buchmeiser, "Carbon Fibers : Precursor Systems , Processing , Structure , and Properties," *Angew. Rev.*, pp. 5262–5298, 2014.

[39] J. F. Snyder, E. B. Gienger, and E. D. Wetzel, "Performance metrics for structural composites with electrochemical multifunctionality," 2015.

[40] M. L. Minus and S. Kumar, "The processing, properties, and structure of carbon fibers," *Jom*, vol. 57, no. 2, pp. 52–58, 2005.

[41] X. Huang, "Fabrication and properties of carbon fibers," *Materials (Basel).*, vol. 2, no. 4, pp. 2369–2403, 2009.

[42] E. Pop, V. Varshney, and A. K. Roy, "Thermal properties of graphene: Fundamentals and applications," *MRS Bull.*, vol. 37, no. 12, pp. 1273–1281, 2012.

[43] D. J. Johnson, "Structure-property relationships in carbon fibres," *J. Phys. D. Appl. Phys.*, vol. 20, no. 3, pp. 286–291, 1987.

[44] G. Fredi *et al.*, "Graphitic microstructure and performance of carbon fibre Li-ion structural battery electrodes," *Multifunct. Mater.*, vol. 1, no. 1, p. 015003, 2018.

[45] V. Serin, R. Fourmeaux, Y. Kihn, J. Sevely, and M. Guigon, "Nitrogen distribution in high tensile strength carbon fibres," *Carbon N. Y.*, vol. 28, no. 4, pp. 573–578, 1990.

[46] L. Laffont, "An EELS study of the structural and chemical transformation of PAN polymer to solid carbon," vol. 42, pp. 2485–2494, 2004.

[47] S. D. Gardner, G. He, and C. U. Pittman, "A spectroscopic examination of carbon fiber cross sections using XPS and ISS," *Carbon N. Y.*, vol. 34, no. 10, pp. 1221–1228, 1996.

[48] S. Duan, F. Liu, T. Pettersson, C. Creighton, and L. E. Asp, "Determination of transverse and shear moduli of single carbon fibres," *Carbon N. Y.*, vol. 158, pp. 772–782, 2020.

[49] Toray, "Types of Carbon Fiber," 2020. [Online]. Available: https://www.toraycma.com/page.php?id=661. [Accessed: 30-Nov-2020].

[50] M. S. Dresselhaus, G. Dresselhaus, K. Sugihara, I. L. Spain, and H. A. Goldberg, *Graphite Fibers and Filaments*, vol. 5, no. 4. Berlin, Heidelberg: Springer Berlin Heidelberg, 1988.

[51] K. Sun, M. A. Stroscio, and M. Dutta, "Graphite C-axis thermal conductivity," *Superlattices Microstruct.*, vol. 45, no. 2, pp. 60–64, 2009.

[52] M. H. Kjell, E. Jacques, and D. Zenkert, "PAN-Based Carbon Fiber Negative Electrodes for Structural Lithium-Ion Batteries," vol. 158, no. 12, pp. 1455–1460, 2011.

[53] J. Hagberg, S. Leijonmarck, and G. Lindbergh, "High Precision Coulometry of Commercial PAN-Based Carbon Fibers as Electrodes in Structural Batteries," *J. Electrochem. Soc.*, vol. 163, no. 8, pp. A1790–A1797, 2016.

[54] E. Jacques, M. Hellqvist Kjell, D. Zenkert, G. Lindbergh, and M. Behm, "Expansion of carbon fibres induced by lithium intercalation for structural electrode applications," *Carbon N. Y.*, 2013.

[55] E. Jacques, M. H. Kjell, D. Zenkert, G. Lindbergh, M. Behm, and M. Willgert, "Impact of electrochemical cycling on the tensile properties of carbon fibres for structural lithium-ion composite batteries," *Compos. Sci. Technol.*, vol. 72, no. 7, pp. 792–798, 2012.

[56] E. Jacques *et al.*, "Impact of Mechanical loading on the electrochemical behaviour of carbon fibres for use in energy storage composite materials," in *18th International Conference on Composite Materials*, 2011, pp. 1–6.

[57] J. C. Woicik, *Hard X-ray Photoelectron Spectroscopy (HAXPES)*. Springer International Publishing, 2016.

[58] A. Jablonski and C. J. Powell, "Practical expressions for the mean escape depth, the information depth, and the effective attenuation length in Auger-electron spectroscopy and x-ray photoelectron spectroscopy," *J. Vac. Sci. Technol. A Vacuum, Surfaces, Film.*, vol.

27, no. 2, pp. 253–261, 2009.

[59] C. Schlueter *et al.*, “The new dedicated HAXPES beamline P22 at PETRA III,” in *AIP Conference Proceedings*, 2019, vol. 2054, no. 040010.

[60] S. Tanuma, C. J. Powell, and D. R. Penn, “Calculations of electron inelastic mean free paths. IX. Data for 41 elemental solids over the 50 eV to 30 keV range,” *Surf. Interface Anal.*, vol. 43, no. 3, pp. 689–713, 2011.

[61] M. B. Trzhaskovskaya and V. G. Yarzhemsky, “Dirac–Fock photoionization parameters for HAXPES applications,” *At. Data Nucl. Data Tables*, vol. 119, pp. 99–174, 2018.

[62] M. K. Miller and R. G. Forbes, *Atom probe tomography and the local electrode atom probe*. Springer, 2014.

[63] O. Nishikawa and M. Taniguchi, “Atomic level analysis of carbon fibers by the scanning atom probe,” *Surf. Interface Anal.*, vol. 46, no. 12–13, pp. 1231–1235, 2014.

[64] R. K. W. Marceau *et al.*, “Local Electrode Atom Probe Tomography of Carbon Fibre,” *Microsc. Microanal.*, vol. 25, no. S2, pp. 2496–2497, 2019.

[65] T. F. Kelly and M. K. Miller, “Atom probe tomography,” *Rev. Sci. Instrum.*, vol. 78, no. 3, 2007.

[66] P. J. Birdseye and D. A. Smith, “The electric field and the stress on a field-ion specimen,” *Surf. Sci.*, vol. 23, no. 1, pp. 198–210, 1970.

[67] K. Thompson, D. Lawrence, D. J. Larson, J. D. Olson, T. F. Kelly, and B. Gorman, “In situ site-specific specimen preparation for atom probe tomography,” *Ultramicroscopy*, vol. 107, no. 2–3, pp. 131–139, 2007.

[68] M. Thuvander *et al.*, “Quantitative atom probe analysis of carbides,” *Ultramicroscopy*, vol. 111, no. 6, pp. 604–608, 2011.